

Petrogenesis of the Late Triassic Biluoxueshan granitic pluton, SW China: Implications for the tectonic evolution of the Paleo-Tethys Sanjiang Orogen

Qi Chen ^a, Changming Wang ^{a,*}, Leon Bagas ^{b,c}, Bin Du ^{a,d}, Kangxing Shi ^a, Lifei Yang ^e, Jiaxuan Zhu ^a, Hongyu Duan ^a

^a State Key Laboratory of Geological Processes and Mineral Resources, China University of Geosciences, Beijing 100083, China

^b Centre for Exploration Targeting, The University of Western Australia, Crawley, WA 6009, Australia

^c Xi'an Center of Mineral Resources Survey, China Geological Survey, Xi'an 710054, China

^d China Non-ferrous Metals Resource Geological Survey, Beijing 100012, China

^e School of Earth Sciences, East China University of Technology, Nanchang 330013, China

ARTICLE INFO

Keywords:

Geochronology

Petrogenesis

Biluoxueshan Pluton

Paleo-Tethyan evolution

Sanjiang Orogen

ABSTRACT

The Sanjiang Orogen is important for us to better understand the tectonic evolution of the Paleo-Tethys Ocean. However, the petrogenesis and tectonic setting of the Late Triassic igneous rocks in the central part of the orogen are poorly understood. In this study, we present new whole-rock elemental and isotopic compositions for the Biluoxueshan Pluton, which consists of quartz diorite, granodiorite, and alkali-feldspar granite. Zircon U-Pb dating yields crystallisation ages of 231 ± 1 Ma for the quartz diorite, 227 ± 1 Ma for the granodiorite, and 227 ± 2 , 224 ± 2 , 222 ± 1 , and 217 ± 3 Ma for alkali-feldspar granites, indicating a prolonged emplacement of the pluton. Quartz diorites are metaluminous, high-potassium calc-alkaline, and magnesian in composition. Granodiorites are characterized by peraluminous composition and the existence of normative-corundum, resembling S-type granite. They have negative zircon $\epsilon_{Hf}(t)$ values (-13 to -10.8) and old Hf crustal model ages (2060–1920 Ma), indicating a Paleoproterozoic crustal source. Alkali-feldspar granites are metaluminous to weakly peraluminous, have higher SiO₂ content, FeO_T/MgO ratio and differentiation index (DI) than other samples, and pronouncedly negative Eu anomalies, which are characteristics of highly fractionated granites. They have narrow $\epsilon_{Hf}(t)$ values of -2.7 to $+2.6$ with corresponding Hf crustal model ages of 1410–1060 Ma, indicating a Mesoproterozoic juvenile crustal source modified by mantle-derived magma. By combining previous and the new data, we proposed a new tectonic evolution model of a Late Triassic northward scissor-like post-collisional extension during ca. 235–223 Ma in the Changning-Menglian Suture Zone.

1. Introduction

The Sanjiang Orogen is at the southeastern margin of the Tibetan Plateau and is considered an important part of the Eastern Tethys-Himalaya zone located between the Gondwana and Eurasia continents (Sengör, 1987, 1990; Metcalfe, 2002, 2013; Deng et al., 2012, 2018; Wang et al., 2015b, 2016). Due to the distinctive tectonic history, widespread igneous rocks, and diverse mineral resources, the Sanjiang Tethyan Orogen has become a focal point for studying the evolution of the Paleo-Tethys Ocean (e.g. Wang et al., 2014b, 2015a, 2018b; Deng et al., 2017; Du et al., 2019). Amongst the sutures recognised in the orogen, the Changning-Menglian Suture Zone (CSZ) is a complex structure aligning with the Longmu Co-Shuanghu Suture Zone (LSZ) to

the north and with the Chiang Mai-Inthanon Suture Zone in Thailand to the south (Fig. 1a). The CSZ and LSZ have experienced a complex process of accretionary and collisional deformation, and are regarded as the main remnants of the Paleo-Tethys Ocean (e.g. Metcalfe, 2002; Li, 2008; Wang et al., 2015b; Deng et al., 2018).

Earlier studies in the CSZ have focused on deciphering the relationship between magmatism and the tectonic evolution from subduction to post-collisional events (Wu et al., 1995; Hennig et al., 2009; Peng et al., 2013). The suture zone consists of high pressure (HP) to ultrahigh pressure (UHP) metamorphic belts, Devonian ophiolitic mélange, Carboniferous to Permian ocean-island mafic volcanism, arc-related igneous rocks, and Middle to Late Triassic plutons and bimodal volcanic units. These studies have helped constrain the opening and closure of

* Corresponding author.

E-mail address: wangcm@cugb.edu.cn (C. Wang).

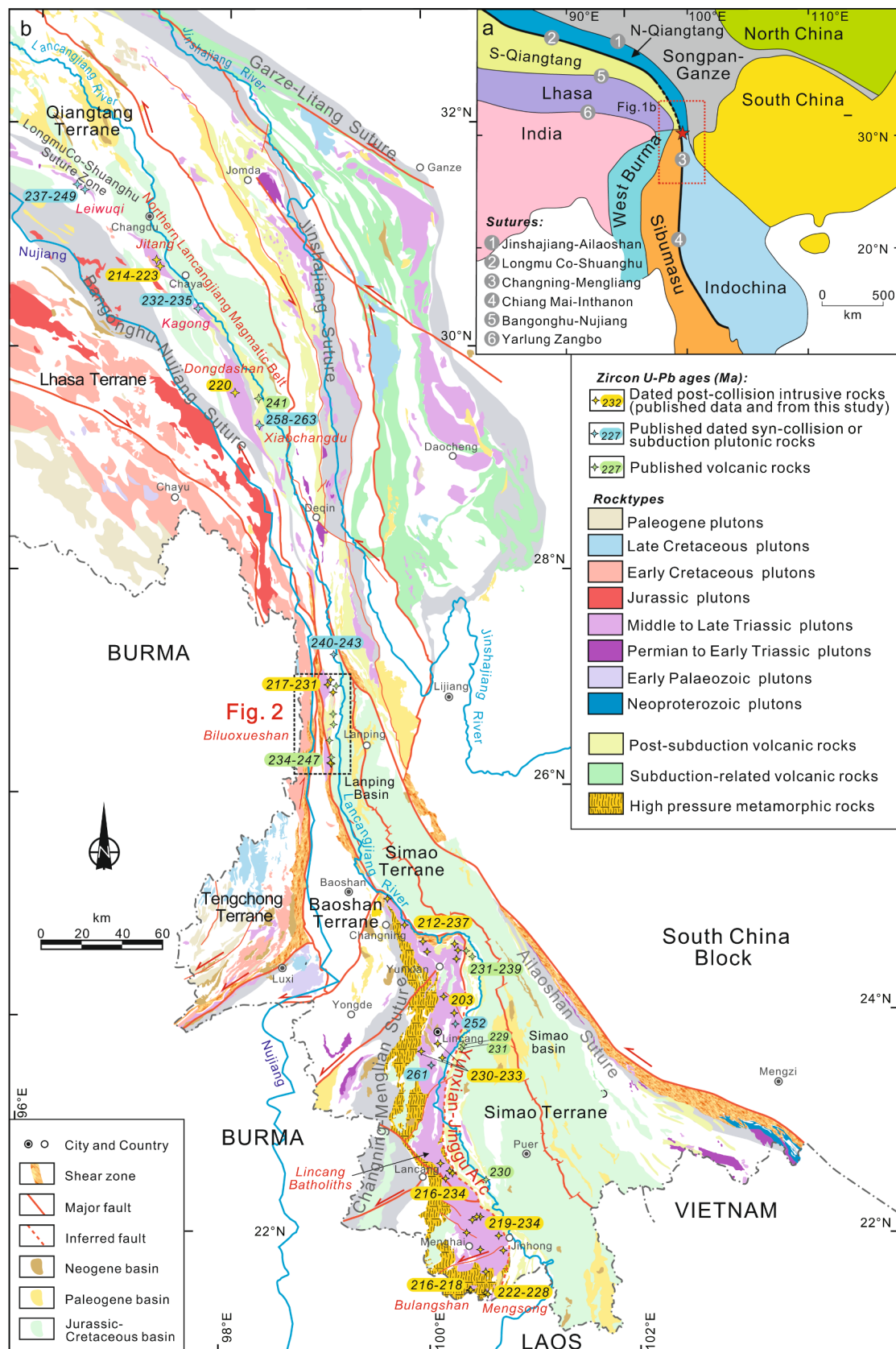


Fig. 1. (a) Simplified tectonic framework of the Sanjiang Orogen and its adjacent areas (modified after Metcalfe, 2002; Wang et al., 2014a). (b) Sanjiang Orogen showing the distribution of Early Paleozoic to Cenozoic igneous rocks and major sutures (modified after Wang et al., 2016; Deng et al., 2019). The zircon U-Pb ages of the igneous rocks are from this study and literature. Data sources are shown in Supplementary Table 1.

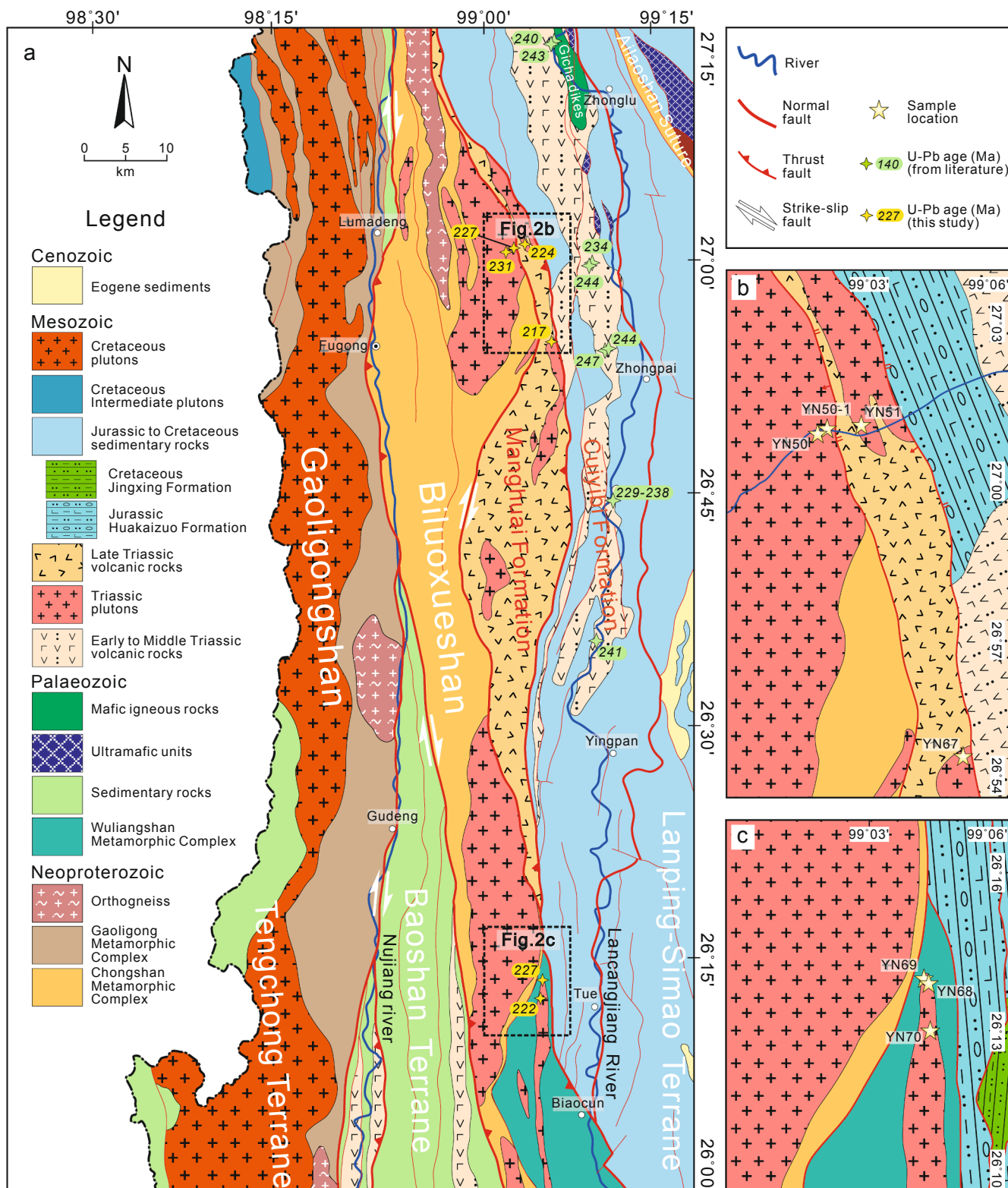


Fig. 2. Geological maps: (a) the Biluoxueshan Pluton and distribution of igneous rocks (modified after YNBGMR, 1990), and locations of dated samples; (b) the sample sites in the northern part of the Biluoxueshan Pluton; and (c) the sample sites in the southern part of the Biluoxueshan Pluton. The zircon U-Pb ages of the surrounding volcanic rocks are listed in Supplementary Table 1.

the Paleo-Tethys Ocean and subsequent accretion and collisional tectonic events (Jian et al., 2009a, 2009b; Wang et al., 2010; Deng et al., 2018; Fan et al., 2015; Zhai et al., 2019; Fig. 1b).

Numerous Permian to Triassic plutons related to the closure of the Paleo-Tethys Ocean were also found along the northern Lancangjiang

Magmatic Belt (LMB) (Hu et al., 2014; Tao et al., 2014; Peng et al., 2015; Wang et al., 2018c; Fig. 1b). Widespread Middle to Late Triassic plutons along the belt provides important aids for us to better understand the tectonic evolution of the continental crust and magmatism (Pitcher, 1983; Pearce et al., 1984; Peng et al., 2013; Sami et al., 2018). However,

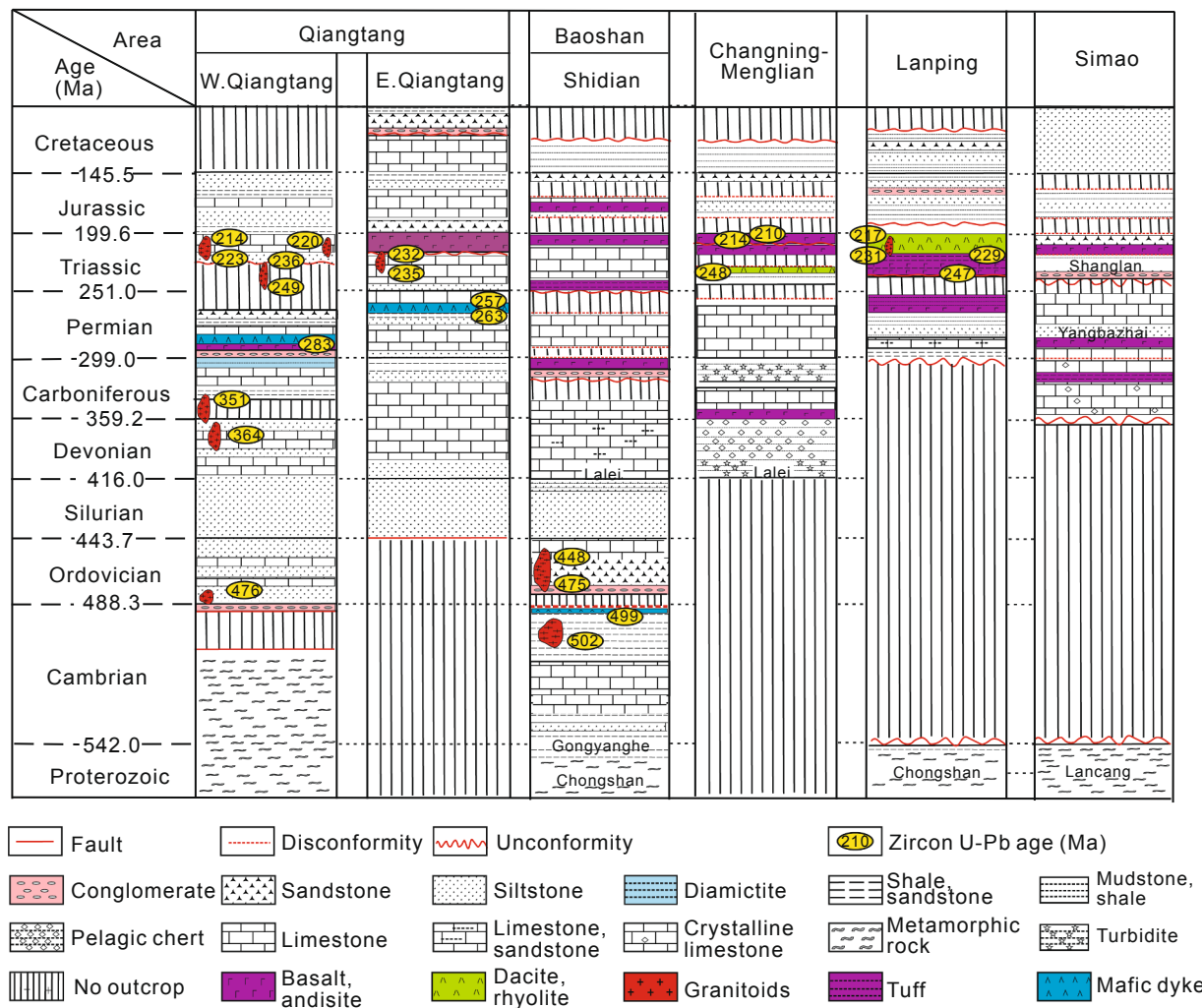


Fig. 3. Generalised time-space stratigraphic successions showing the oldest metamorphic rocks, sedimentary cover, and tectono-magmatic history of different subterraneans in the middle Sanjiang Orogen (modified after Cohen et al., 2013; Wang et al., 2015b). Thickness of different unit are not drawn to scale.

the petrogenesis and tectonic setting of the Late Triassic plutons along the belt are still poorly understood, which hinders our understanding of the syn- to post-collision events following the closure of the Paleo-Tethys Ocean.

The north-trending Biluoxueshan Pluton extends for over 200 km, and is ideal for investigating the petrogenesis of the igneous rocks in the Paleo-Tethys Ocean. Several studies have focused on transpressive deformation (Zhang et al., 2012), geochemical characteristics of granitoids (Luo et al., 2016), and continental arc-volcaniclastics in this region (Fan et al., 2014; Su et al., 2014; Yang et al., 2014; Yang et al., 2020). Yet the geochronology and geochemistry of the Biluoxueshan Pluton have not been studied in any detail due to the difficulties to access. Given that the Biluoxueshan Pluton is important, we have chosen this pluton for detailed studies of petrology, whole-rock geochemistry, zircon U-Pb and Lu-Hf isotopic geochemistry. The aim of this paper is to provide new constraints on the petrogenesis of the pluton and tectonic evolution of the Paleo-Tethys Ocean in the middle part of the Sanjiang Orogen.

2. Geological setting and petrology

2.1. Geological background

The Sanjiang Orogen in southwestern China includes several terranes separated by sutures recording collisional events related to the

Palaeozoic to Mesozoic closure of the Paleo-Tethys Ocean and the final collision of the Indian and Eurasian continents during the Cenozoic (Deng et al., 2019; Wang et al., 2016; Fig. 1a). The Paleo-Tethys Ocean during that period can be divided into the Longmu Co-Shuanghu Ocean between the North and South Qiangtang terranes in eastern part of the Tibetan Plateau, and the Changning-Menglian Ocean between the Simao and Baoshan terranes in the western part of the Yunnan Province (Cong et al., 1993; Zhong, 1998). Abundant Triassic igneous rocks crop out discontinuously along both sides of the LMB, forming an elongated magmatic belt subparallel to Paleo-Tethys sutures (Mo et al., 1993, 1994; Zhong, 1998; Metcalfe, 2002, 2013; Li, 2008; Jian et al., 2009a, 2009b; Peng et al., 2013; Fig. 1b). Although no ophiolitic or HP-UHP rocks have been recognised in the LMB to the central Qiangtang Terrane, many Triassic plutons and volcanic rocks have been documented along the western margin of the eastern Qiangtang Terrane (Hu et al., 2014; Tao et al., 2014; Peng et al., 2015; Wang et al., 2018c; Chen et al., 2019; Fan et al., 2020).

The Changning-Menglian Ocean began opening in the Middle Devonian and subducted beneath the Simao Terrane during the Late Carboniferous to Middle Permian. The Paleo-Tethys Ocean closed before ca. 252 Ma (Deng et al., 2018). The subsequent collision during the Middle Permian to Middle Triassic established the CSZ (Mo et al., 1993, 1994; Hennig et al., 2009; Jian et al., 2009a; Wang et al., 2015b; Deng et al., 2018). Late Triassic igneous rocks during the emplacement of batholiths in the CSZ, such as the Lincang, Mengsong and Bulangshan

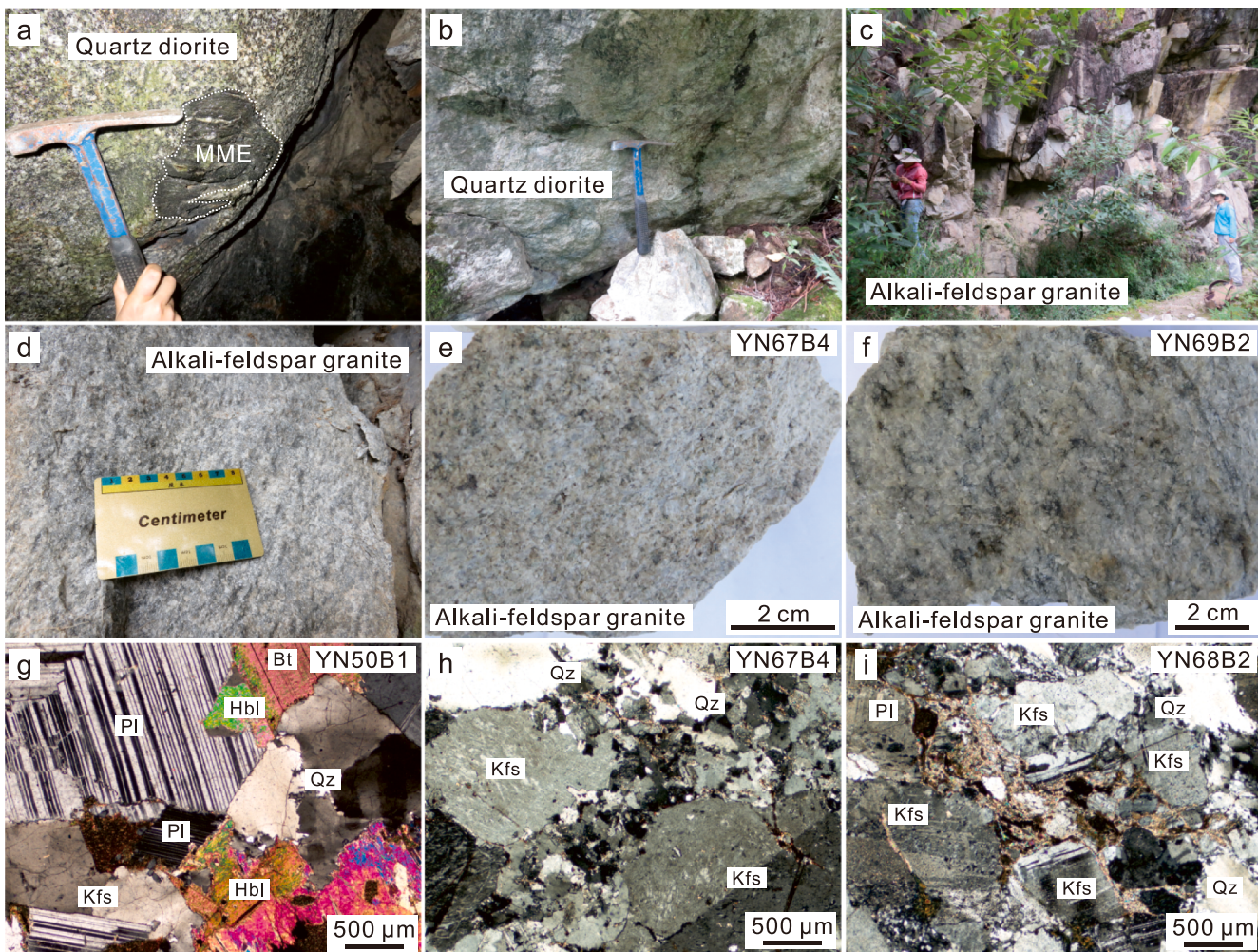


Fig. 4. Field photographs: (a)–(d) the Late Triassic granitoids in the Biluoqeshan Pluton; (e)–(f) hand specimens of the alkali-feldspar granite; (g)–(i) thin section photomicrographs showing the textural features and mineral compositions of samples. Abbreviations: Bt = biotite; Hbl = hornblende; Kfs = K-feldspar; Pl = plagioclase; Qz = quartz.

batholiths, relate to syn- and post-collisional orogenic events (Wu et al., 1995; Hennig et al., 2009; Dong et al., 2013; Peng et al., 2013; Wang et al., 2015b; Deng et al., 2018; Cong et al., 2020).

2.2. Biluoqeshan Pluton

The Biluoqeshan Pluton is in the centre of the Sanjiang Orogen and extends southward to the Lincang batholith of the CSZ (Fig. 1b). The eastern part of the pluton borders the Lanping-Simao Terrane in the Indochina Block, which is part of the Cathaysian Continent (Wu et al., 1995; Fig. 2a). The Lanping-Simao Terrane extends eastward to the Jinshajiang-Ailaoshan Suture Zone, which is interpreted as a back-arc basin related to the Paleo-Tethys Ocean (Wang et al., 2000). Thick Paleozoic to Mesozoic supracrustal successions unconformably overlie the Proterozoic rocks in the region (Wang et al., 2015b). The Late Palaeozoic units consist of shelf facies clastic carbonate rocks interbedded with mafic volcanics (Wang et al., 2015b, 2018a; Zhang et al., 2017; Yang et al., 2019, 2020; Fig. 3).

The Baoshan Terrane to the west of the study area is part of the Gondwana Supercontinent (Wu et al., 1995), where widespread Proterozoic HP metamorphic rocks are exposed discontinuously along the Chongshan and Gaoligongshan metamorphic complexes (YNBGMR, 1990). The Chongshan Metamorphic Complex is subdivided into low-

grade metasedimentary rocks to the east and amphibolite- to granulite-facies gneiss to the west (Zhang et al., 2012).

Cambrian units in the region are overlain unconformably by Early Ordovician conglomerate and shallow- to deep-marine sedimentary rocks followed by Silurian to Carboniferous shallow-marine sedimentary beds interfingering with continental beds, which are intruded by the Biluoqeshan Pluton (YNBGMR, 1990; Wang et al., 2015b). Given that three tectonic sutures converge at the Biluoqeshan Pluton, the tectonic evolution of the granitoids in the pluton has been affected by the Mesozoic closure of the Paleo-Tethys Ocean and subsequent continental collision, and by escape structures and continuous widespread strike-slip faults related to the Cenozoic Himalayan Orogeny (Cong et al., 1993; Zhong, 1998; Pan et al., 2003; Deng et al., 2012, 2017).

The Biluoqeshan Pluton also intrudes the Paleoproterozoic Chongshan Metamorphic Complex and Late Triassic Manghuai Formation bimodal volcanics (Fig. 2a). The northern end of the pluton, which is also named the Laowoshan Pluton (YNBGMR, 1990), is in fault contact with the Middle Jurassic Huakaizuo Formation and Triassic volcanics (Fig. 2b). The southern end of the pluton is in fault contact with the Early Cretaceous Jingxing and Middle Jurassic Huakaizuo formations (Fig. 2c).



Fig. 5. Cathodoluminescence images of representative zircons from the Late Triassic quartz diorite, granodiorite, and alkali-feldspar granite from the Biluoqueshan Pluton. The larger green circles represent the spots of Lu-Hf analysis, and the smaller red circles represent the spots of U-Pb analysis, corresponding to U-Pb age in Ma and the $\epsilon_{Hf}(t)$ values are shown below of the zircons. (For interpretation of the references to colour in this figure legend, the reader is referred to the web version of this article.)

2.3. Petrography

The multiple phases recognised in the Biluoqueshan Pluton by this study are compositionally quartz diorites, granodiorites, and alkali-feldspar granites. The quartz diorites and granodiorites are exposed in the northern part of the pluton, and the alkali-feldspar granites are elongated in a N-S direction and is in faulted contact with Mesozoic units in the pluton (Fig. 2a).

The quartz diorite is grey, medium-grained, equigranular, and contains dark enclaves (Fig. 4a, b). The quartz diorite consists of ~40 vol% plagioclase, ~20 vol% hornblende, ~15 vol% K-feldspar, ~15 vol% quartz, ~10 vol% biotite, and the accessory minerals apatite, magnetite and sphene that constituting < 1 vol% of the rock (Fig. 4g). The granodiorite is grey, typically equigranular, and consist of ~20 vol% K-feldspar, ~40 vol% plagioclase, ~30 vol% quartz, ~5 vol% biotite, ~5 vol% hornblende, and the accessory minerals apatite and Fe-Ti oxides that total < 1 vol% of the rock. The alkali-feldspar granite is greyish white, equigranular and composed of ~50 vol% K-feldspar, ~30 vol% quartz, ≤ 10 vol% plagioclase, ~10 vol% biotite, and < 1 vol% accessory minerals including apatite and zircon (Fig. 4c–f). The K-feldspar grains range in size between 0.5 and 2 mm long with Carlsbad twinning and weak sericitic and kaolinic alteration (Fig. 4h, i).

3. Analytical method

3.1. Zircon U-Pb dating

Zircon grains were collected from the samples involving crushing,

and using conventional heavy liquid and magnetic separation methods followed by hand picking under a binocular microscope. The grains were mounted on adhesive tape, enclosed in epoxy resin, then polished to expose their crystal centre and coated with carbon for analysis. Before the analysis of zircon, cracks, oscillatory zoning, and inclusion were observed in the zircons on cathodoluminescence (CL) images.

Zircon U-Pb geochronology was analysed using a laser-ablation inductively-coupled-plasma mass spectrometry (LA-ICP-MS) at the State Key Laboratory of Continental Dynamics, Northwest University, Xi'an, China. The chosen zircons were ablated with an Agilent 7500 Inductively Coupled Plasma Mass Spectrometer (ICP-MS) equipped with a 193 nm ArF Excimer Laser Ablation System forming a spot with a diameter of 35 μm at a frequency of 10 Hz. The standard 91500 (with a weighted mean $^{206}\text{Pb}/^{238}\text{U}$ age of 1062.4 ± 5.9 Ma; 2σ) and GJ-1 standard (with a weighted mean $^{206}\text{Pb}/^{238}\text{U}$ age of 599.5 ± 4.0 Ma; 2σ) zircons were used to monitor the ages of unknowns. The isotopic ratios and element contents of the sample were calculated applying the Glitter 4.0 data reducing software, and common Pb contents were measured using the method described by Andersen (2002). Age calculations and concordia diagrams were constructed applying the ISOPLOT Version 3.0 software (Ludwig, 2003). The uncertainties for individual analyses are quoted at the 2σ level, and the errors in the weighted mean ages are at the 95% confidence level.

3.2. Whole-rock geochemistry

Analyses of major and trace element contents of the samples from the Biluoqueshan Pluton were completed at the National Research Center

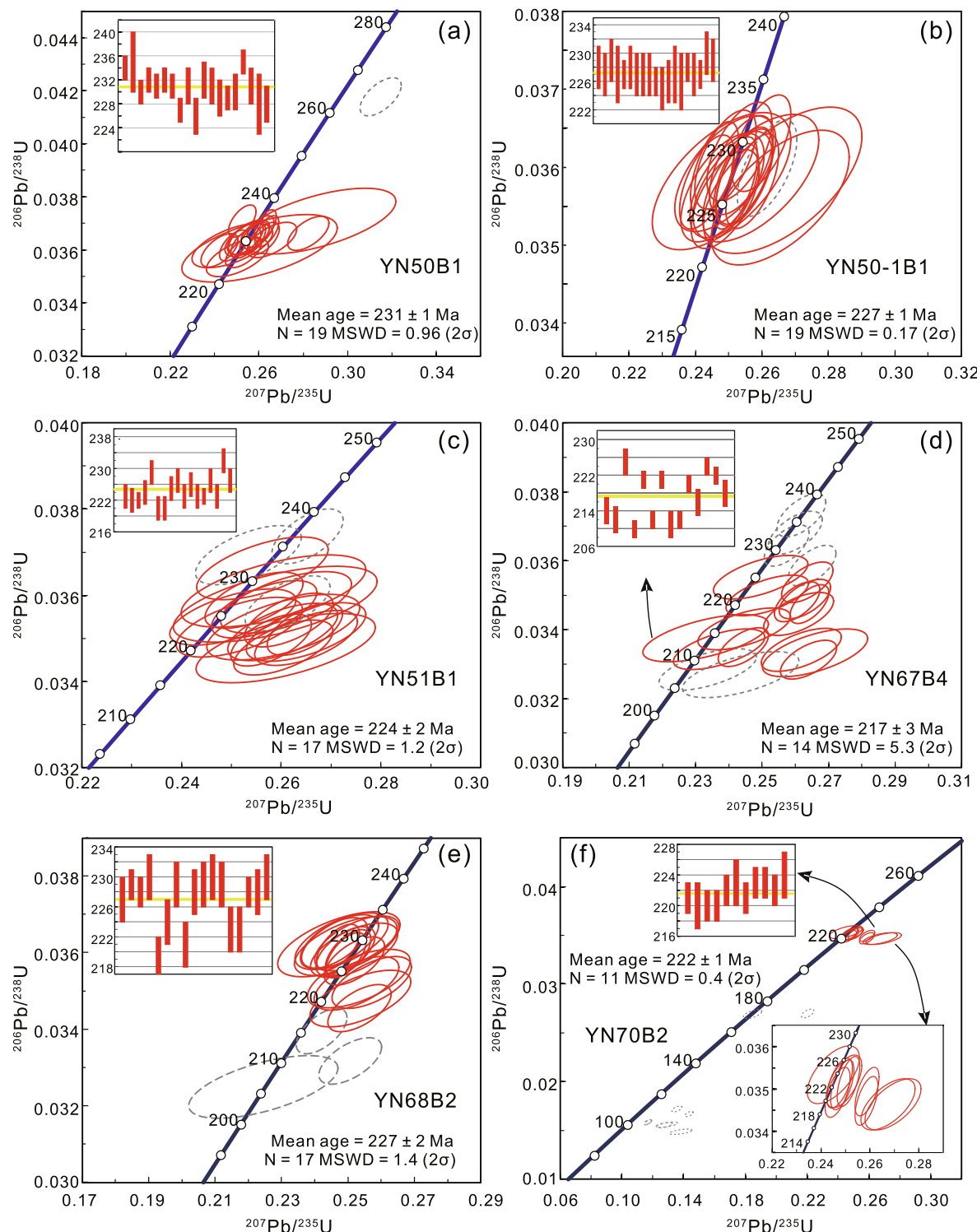


Fig. 6. Zircon U-Pb concordia plots for samples from the Biluoxueshan Pluton: (a) quartz diorite; (b) granodiorite; and (c)–(f) alkali-feldspar granite.

for Geoanalysis, Beijing, China. The samples were crushed to a < 200 mesh size in a tungsten-carbide ball mill. The X-ray fluorescence (XRF) spectrometer (PW4400) was used to assay the major element analyses. The trace elements including rare earth elements (REEs) were assayed using an inductively-coupled-plasma mass spectrometry (ICP-MS, model number: PE300D) attached to a Finnigan MAT (Element I) instrument. The errors in the XRF analysis are estimated to be $< 1\%$ for SiO_2 and $< 2\%$ for the other major oxides. The ICP-MS analyses yield accuracies

better than 5% for most elements by multiple analyses of standards.

3.3. Zircon Hf isotope

In situ zircon Hf isotopic analyses were completed using a Neptune Plus MC-ICP-MS in combination with a Geolas 2005 excimer ArF laser ablation system, at the State Key Laboratory of Geological Processes and Mineral Resources, China University of Geosciences, Wuhan. The Lu-Hf

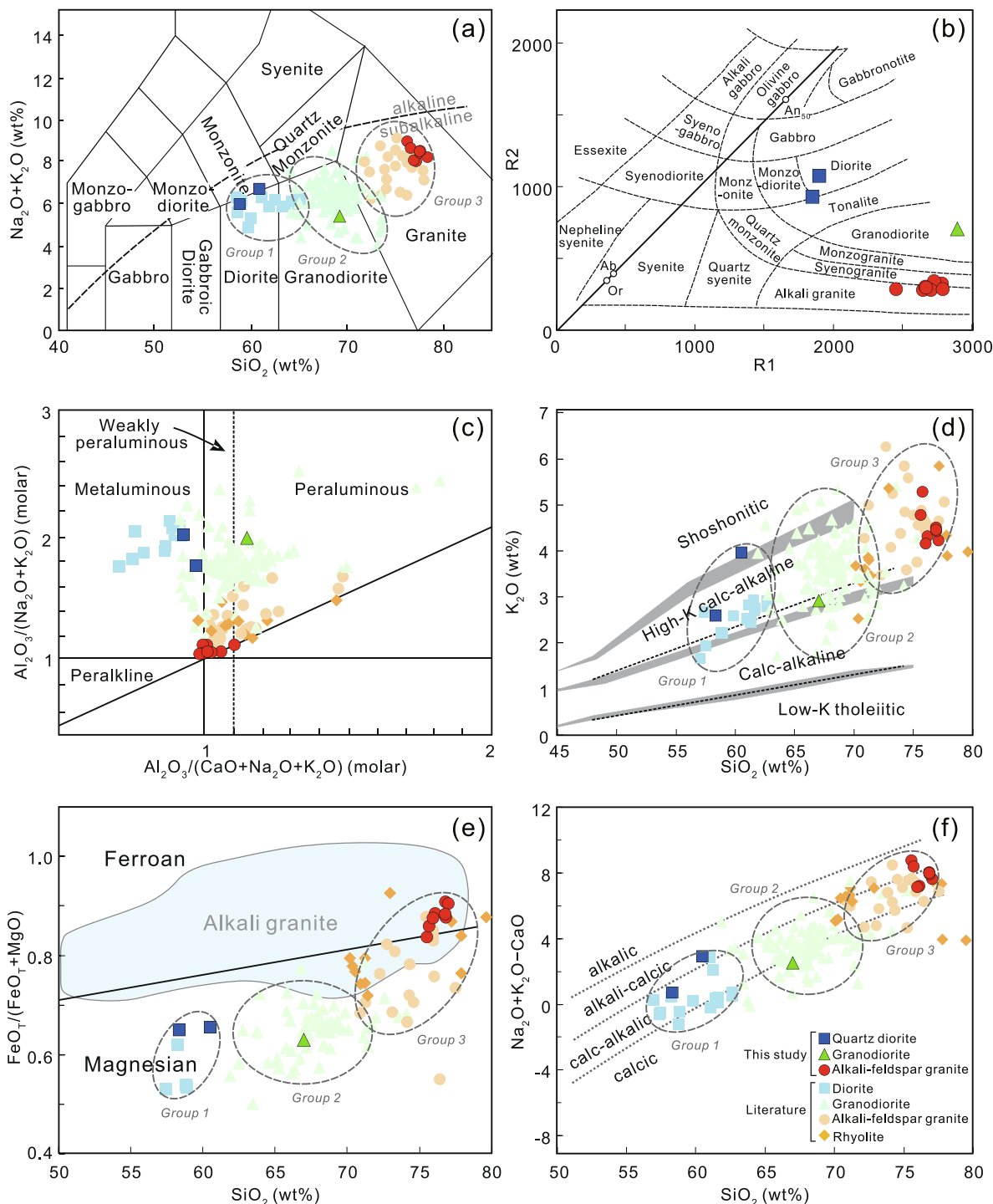


Fig. 7. Granitic classification diagrams for samples from the Biluoqueshan Pluton: (a) Total Alkali Silica (TAS) classification plot (after Middlemost, 1994); (b) R2 vs R1 plot (after De la Roche et al., 1980); (c) A/NK vs A/CNK plot (after Frost et al., 2001); (d) K_2O vs SiO_2 plot (after Rickwood, 1989); (e) $\text{FeO}_T / (\text{FeO}_T + \text{MgO})$ vs SiO_2 plot (after Frost et al., 2001); and (f) Modified Alkali-lime Index (MALI = $\text{Na}_2\text{O} + \text{K}_2\text{O} - \text{CaO}$) vs SiO_2 plot (after Frost et al., 2001). The published data for the Late Triassic igneous rocks in the CSZ are listed in Supplementary Table 1, and the LSZ are from Li et al. (2015), Liu et al. (2016), Zhao et al. (2018b), and Xu et al. (2020).

isotopic analyses were carried out with the laser ablation beam set at a diameter of 44 μm , an 8–10 Hz repetition rate, and 5.3 J/cm² in energy density on neighbouring zones where the U-Pb analyses were performed. Helium was used as a carrier in the ablation cell and merged with argon after the ablation cell (Hu et al., 2008a, 2008b). Detailed instrumental conditions of the laser ablation system and the data acquisition procedures are presented in Hu et al. (2012).

4. Results

4.1. Zircon LA-ICP-MS U-Pb dating

The LA-ICP-MS zircon U-Pb isotope data for quartz diorite (Sample YN50B1), granodiorite (Sample YN50-1B1), and alkali-feldspar granite (Samples YN51B1, YN67B4, YN68B2, and YN70B2) are presented in Supplementary Table 2. Representative cathodoluminescence (CL)

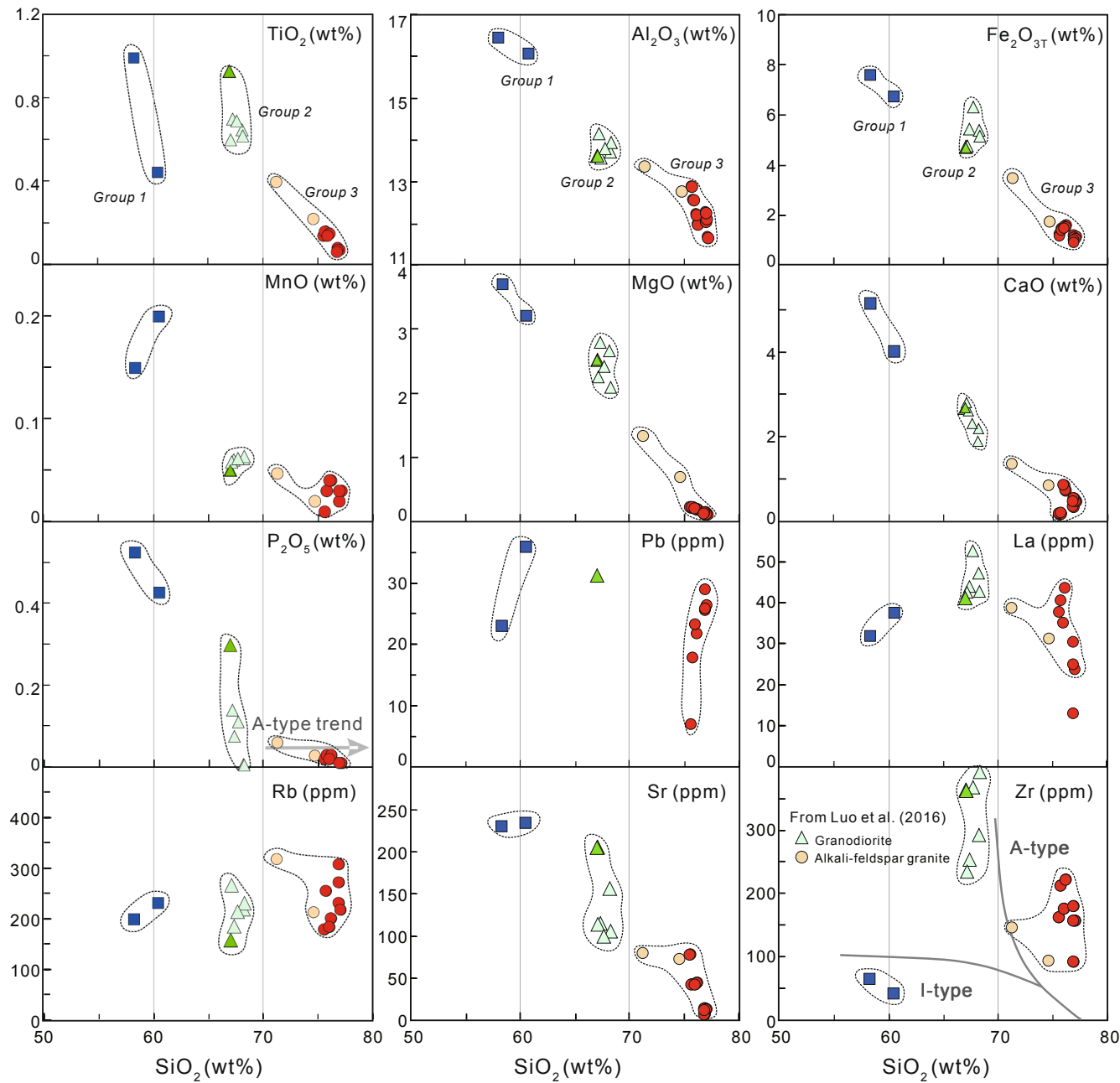


Fig. 8. Harker diagrams for samples of multiple phases from the Biluoxueshan Pluton. Published data are from [Luo et al. \(2016\)](#).

images and U-Pb concordia plots are shown in [Figs. 5 and 6](#).

Zircons crystals from the quartz diorite are typically transparent and euhedral in shape, and between 100 and 300 μm long with length-to-width ratios of between 1:1 and 3:1. Oscillatory zoning is common in most colourless to grey crystals ([Fig. 5a](#)). Twenty zircons were analysed containing 181–778 ppm Th and 624–12,378 ppm U, with Th/U ratios between 0.06 and 0.66. These values for the zircons together with their REE patterns shown in [Supplementary Fig. S1](#), are characteristic of magmatic zircons with one zircon (Spot 17) being xenocrystic ([Hoskin and Schaltegger, 2003](#)). The 19 youngest dated spots are concordant and give a weighted mean $^{206}\text{Pb}/^{238}\text{U}$ age of 231 ± 1 Ma interpreted as the crystallisation age of the quartz diorite ([Fig. 6a](#); MSWD = 0.96, n = 19, 2σ).

The Chondrite-normalised REE patterns for zircons from the granodiorite are presented in [Supplementary Fig. S1](#). The zircons are typically

euhedral and long prismatic crystals measuring between 150 and 300 μm long with length-to-width ratios of 2:1–3:1. Most of the crystals are colourless to dark grey on the CL images and exhibit well-defined oscillatory zoning typical of magmatic zircons ([Fig. 5b](#)). Twenty zircons assay 181–747 ppm Th and 443–1826 ppm U, with Th/U ratios between 0.17 and 0.82. Except for a hydrothermal zircon (Spot 18), the analyses form a single, tight cluster on the concordant plot yielding a weighted mean $^{206}\text{Pb}/^{238}\text{U}$ age of 227 ± 1 Ma, which is interpreted as the crystallisation age of the granodiorite ([Fig. 6b](#); MSWD = 0.17, n = 19, 2σ).

Zircons from the alkali-feldspar granite (Sample YN51B1) are colourless, transparent, and form subhedral prismatic crystals ranging between 50 and 150 μm long with length-to-width ratios of between 1:1 and 1.5:1. These zircons exhibit well-defined oscillatory zoning on the CL images ([Fig. 5c](#)). Twenty zircons assay 281–5847 ppm Th and

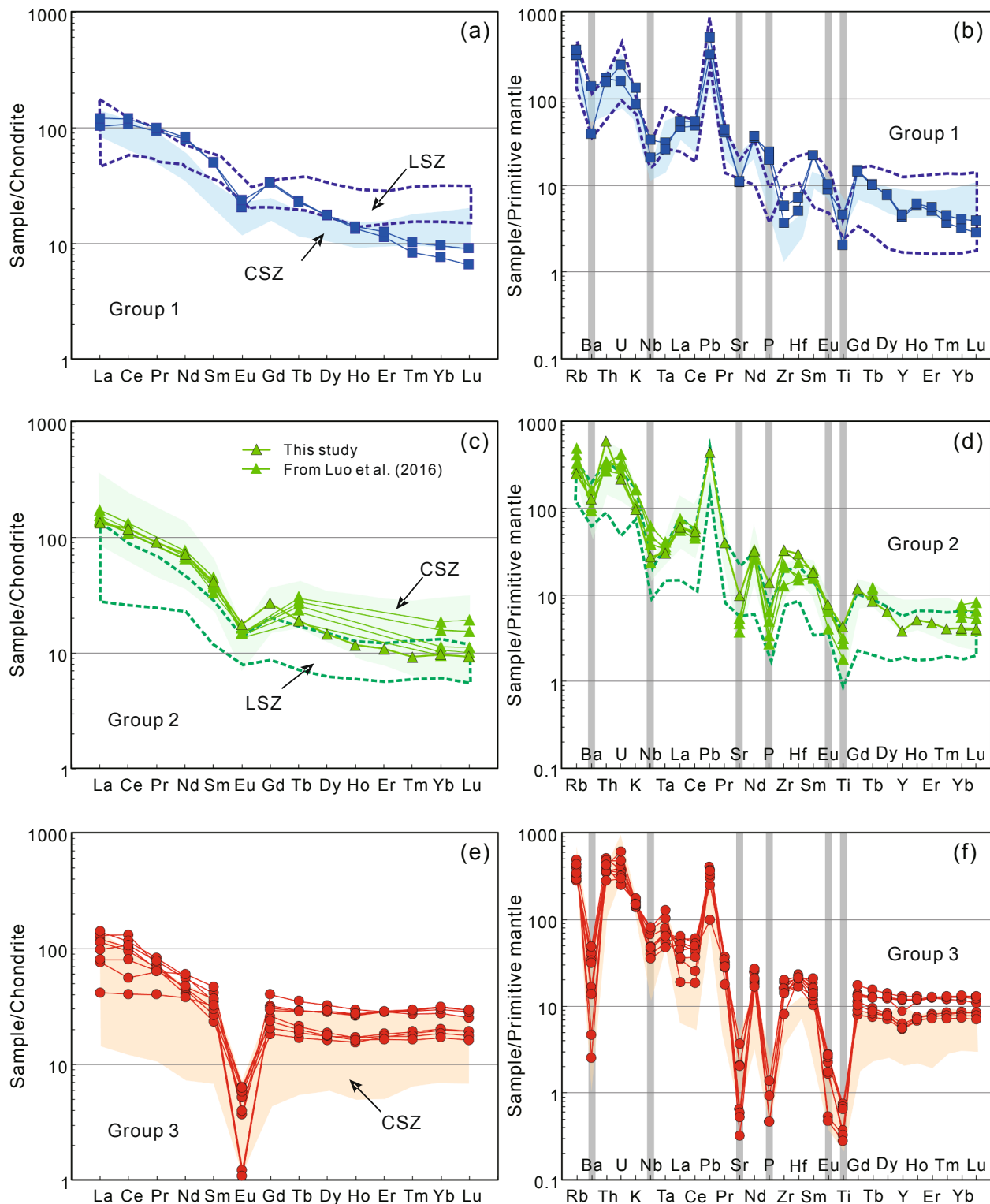


Fig. 9. Normalised plots for the multiple phases sampled from the Biluoqueshan Pluton: (a) Chondrite-normalised REE patterns; and (b) primitive mantle-normalised trace element spider diagrams. The Chondrite and primitive mantle data are from Sun and McDonough (1989). The light blue, green and orange fields represent post-collisional granites in the CSZ (Supplementary Table 1), and the blue and green dotted area represent post-collisional granites in the LSZ (Li et al., 2015; Liu et al., 2016; Zhao et al., 2018b; Xu et al., 2020). (For interpretation of the references to colour in this figure legend, the reader is referred to the web version of this article.)

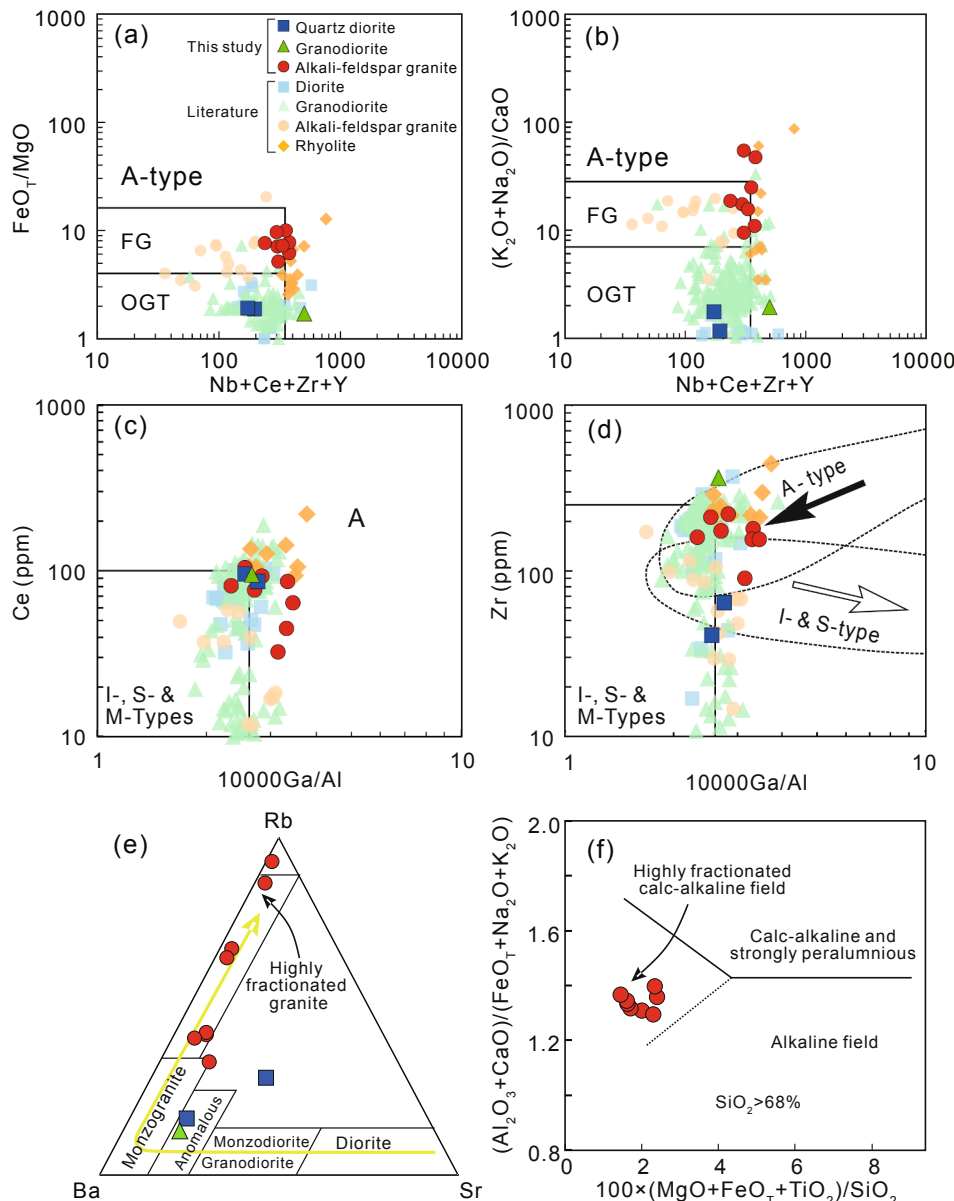


Fig. 10. Discrimination and classification diagrams for samples from the Biluoxueshan Pluton: (a)–(d) Discrimination diagrams for A-type granites (after Whalen et al., 1987; Frost et al., 2001); (e) triangular Rb–Ba–Sr diagram (after Wang et al., 2013); (f) major element classification diagram ($\text{SiO}_2 > 68\%$), showing the fields of alkaline, calc-alkaline, and highly fractionated calc-alkaline rocks (after Sylvester, 1989). Abbreviations: FG = fractionated M-, I- and S-type granites; OGT = unfractionated M-, I- and S-type granites. Symbols are the same as in Fig. 7.

763–5822 ppm U (with the Th/U ratios varying from 0.34 to 1.35). Except for zircon Spots 10, 12, and 20, which are interpreted as hydrothermal zircons based on their LREE enrichment, minor or no Ce and Sm anomalies and negative Eu anomaly (Supplementary Fig. S1), 17 magmatic zircons yield a concordant weighted mean $^{206}\text{Pb}/^{238}\text{U}$ age of 224 ± 2 Ma interpreted as the crystallisation age of the alkali-feldspar granite (Fig. 6c; MSWD = 1.2, n = 17, 2 σ).

Zircons from the alkali-feldspar granite (Sample YN67B4) are typically colourless to dark grey euhedral and long prismatic crystals with oscillatory zoning, which are between 100 and 200 μm long with length-to-width ratios of between 1.5:1 and 3:1 (Fig. 5d). Twenty zircons assay 295–1427 ppm Th and 648–2298 ppm U with the Th/U ratios between 0.44 and 0.62. Except for four xenocrystic zircons (Spots 4, 5, 11, and 14) and the two youngest zircons (Spots 12 and 20) interpreted as being discordant, 14 zircons yield a weighted mean $^{206}\text{Pb}/^{238}\text{U}$ age of 217 ± 3 Ma interpreted as the crystallisation age of the alkali-feldspar granite (Fig. 6d; MSWD = 5.3, n = 14, 2 σ).

Zircons from alkali-feldspar granite (Sample YN68B2) are colourless and transparent forming 50–150 μm long euhedral prismatic crystals

with length-to-width ratios of between 1:1 and 2:1. These zircon grains exhibit well-defined oscillatory zoning on the CL images (Fig. 5e). Twenty zircons assay 176–3318 ppm Th and 437–7796 ppm U with the Th/U ratios varying from 0.24 to 0.84. These data, combined with the REE patterns shown in Supplementary Fig. S1, show that the zircons have a magmatic origin. Except for the three apparent youngest zircons (Spots 7, 9, and 16) with discordant dates of ca. 215, 210, and 206 Ma, 17 concordant zircons yield a weighted mean $^{206}\text{Pb}/^{238}\text{U}$ age of 227 ± 2 Ma, which is interpreted as the crystallisation age of the alkali-feldspar granite (Fig. 6e; MSWD = 1.4, n = 17, 2 σ).

The zircon grains in alkali-feldspar granite (Sample YN70B2) are opaque and subhedral to anhedral crystals, and are 50–150 μm long with length-to-width ratios of between 1:1 and 1.5:1. Most of the zircon grains are very dark with indistinct oscillatory zoning on the CL images due to their abnormal high Th (819–29319 ppm) and U (2110–34274 ppm) contents (Fig. 5f). Twenty zircons have Th/U ratios between 0.22 and 1.39. Eleven zircons yield a weighted mean $^{206}\text{Pb}/^{238}\text{U}$ age is 222 ± 1 Ma, and the other spots yield younger ages that are interpreted as unreliable due to radiogenic lead loss (Fig. 6f; MSWD = 0.4, n = 11, 2 σ).

4.2. Geochemistry

The geochemical data for the samples analysed from the Biluo-xueshan Pluton are shown in Supplementary Table 3 and Figs. 7–9. The samples have a wide range of chemical compositions and can be divided into three groups based on their petrology and elemental variations (Fig. 7). Group 1 includes two quartz diorites. The granodiorite is assigned to Group 2, and Group 3 includes alkali-feldspar granites. In addition, published geochemical data of granodiorite collected by Luo et al. (2016) from plutons in the region are included in this study. All the samples have low loss on ignition with values between 0.44 and 2.44 wt %, which are considered to reflect minimal weathering and hydrothermal alteration, and are thus regarded as being fresh enough for further studies (c.f. Karsli et al., 2007).

Group 1 is characterised by low contents of 58.30–60.47 wt% SiO₂ and 5.93–6.98 wt% Na₂O + K₂O, and relatively high contents of 0.44–0.99 wt% TiO₂, 16.17–16.48 wt% Al₂O₃, 6.81–7.68 wt% Fe₂O_{3T}, 3.25–3.75 wt% MgO, 0.15–0.20 wt% MnO, 4.02–5.15 wt% CaO, and 0.43–0.53 wt% P₂O₅ than those of other samples. The samples plot in the diorite to monzodiorite fields on the TAS and R1 vs R2 diagrams (Fig. 7a, b). All samples are metaluminous with A/CNK (molar Al₂O₃/(CaO + K₂O + Na₂O)) ratios of 0.93–0.98, and plot in the high-K calc-alkaline to shoshonitic fields (Fig. 7c, d). Samples in Group 1 plot in the magnesian field on the FeO_T/(FeO_T + MgO) vs SiO₂ diagram (Fig. 7e). The quartz diorites plot in the calc-alkalic to alkali-calcic fields on the modified alkali lime index (MALI) vs SiO₂ diagram (Fig. 7f).

Group 2 has higher SiO₂ (67–68.26 wt%), TiO₂ (0.6–0.93 wt%) and Al₂O₃ (13.6–14.2 wt%), low MnO (0.05–0.06 wt%), MgO (2.11–2.83 wt %), CaO (1.87–2.80 wt%), P₂O₅ (0.01–0.3 wt%) and Na₂O + K₂O (5.23–7.58 wt%) contents compared to other samples, and plots in the granodiorite field on the TAS and R1 vs R2 diagrams (Fig. 7a, b). The samples are peraluminous with A/CNK values of 1.15–1.26 and plot in the calc-alkaline to high-K calc-alkaline fields (Fig. 7c, d). The granodiorites also plot in the magnesian field on the FeO_T/(FeO_T + MgO) vs SiO₂ diagram, and in the calcic to calc-alkaline fields on the MALI vs SiO₂ diagram (Fig. 7e, f).

Among all samples, Group 3 has the highest SiO₂ (75.57–77.06 wt%) and Na₂O + K₂O (7.88–8.85 wt%) contents, and low TiO₂ (0.06–0.16 wt %), Al₂O₃ (11.7–12.93 wt%), MnO (0.01–0.04 wt%), MgO (0.11–0.22 wt%), CaO (0.16–0.84 wt%) and P₂O₅ (0.01–0.03 wt%) contents. The samples plot in the granite field on the TAS diagram and syenogranite to alkali-feldspar granite fields on the R1 vs R2 diagram (Fig. 7a, b). They are weakly peraluminous with A/CNK values of 0.99–1.11, plot in the high-K calc-alkaline, and alkali-calcic to calc-alkalic fields (MALI = 7.10–8.69 wt%; Fig. 7c, d, f), and are ferroan with FeO_T/(FeO_T + MgO) values of 0.84–0.91 (Fig. 7e). On the Harker diagrams in Fig. 8, the TiO₂, Al₂O₃, Fe₂O_{3T}, MnO, MgO, and CaO contents for the samples are inversely proportional to the SiO₂ contents.

The Chondrite-normalised REE plots and primitive mantle-normalised trace element spider diagrams are shown in Fig. 9. The samples from Group 1 and 2 exhibit similar trends on the Chondrite-normalised REE plots, LREE enrichment and HREE (LREE/HREE = 4.64–5.6) depletion (Fig. 9a, c). The groups have high total REE values of 229–249 ppm, Chondrite (La/Yb)_N values of 12.61–13.68, and moderate Eu negative anomalies ($\delta\text{Eu} = 0.48\text{--}0.57$). Group 1 is also moderately enriched in large ion lithophile elements (LILEs), depleted in high field strength elements (HFSEs), and displays negative Ba, Nb, Ta, Sr, and Ti anomalies (Fig. 9b). Group 2 differs from Group 1 in displaying positive Pb, Zr and Hf anomalies, and negative Ba, Nb, Ta, Sr and Ti anomalies in the primitive mantle-normalised spider diagrams (Fig. 9d).

The alkali-feldspar granites (Group 3) differ from the other groups in having “seagull” patterns with fractionated LREEs, pronounced negative Eu anomalies ($\delta\text{Eu} = 0.04\text{--}0.25$), and have relatively flat to weakly enriched LREE patterns with LREE/HREE values of 0.89–3.85 (Fig. 9e). The samples are also enriched in Rb, Th, U, Pb, Ta, Zr, and Hf, and

pronouncedly depleted in Ba, Nb, Sr, P, Eu, and Ti on the primitive mantle-normalised spider plots (Fig. 9f).

4.3. Zircon Lu-Hf isotopes

Zircons from Samples YN50-1B1, YN51B1, and YN68B2 were analysed for Lu-Hf isotopes on or next to U-Pb dated spots (Supplementary Table 4 and Fig. 12). The initial $^{176}\text{Hf}/^{177}\text{Hf}$ ratios were calculated using the neighbouring LA-ICP-MS zircon U-Pb dates.

Nine analyses of zircons from the granodiorite (Sample YN50-1B1) yield initial $^{176}\text{Hf}/^{177}\text{Hf}$ values between 0.282273 and 0.282339, and $\epsilon_{\text{Hf}}(t)$ values between -13 and -10.8, corresponding to two-stage depleted mantle model ages (T_{DM}^{C}) of 2060–1916 Ma (Fig. 12a, b). Ten analyses of zircons from the alkali-feldspar granite (Sample YN51B1) yield initial $^{176}\text{Hf}/^{177}\text{Hf}$ ratios between 0.282610 and 0.282719, and $\epsilon_{\text{Hf}}(t)$ values of -1.3 to +2.6, corresponding to T_{DM}^{C} ages of 1311–1064 Ma (Fig. 12a, b). The analyses of zircons from the alkali-feldspar granite (Sample YN68B2) yield initial $^{176}\text{Hf}/^{177}\text{Hf}$ ratios between 0.282565 and 0.282669, and $\epsilon_{\text{Hf}}(t)$ values of -2.7 to +1, corresponding to T_{DM}^{C} ages of 1408–1173 Ma (Fig. 12a, b).

5. Discussion

5.1. Geochronology of the Biluo-xueshan Pluton

Triassic syn- and post-collisional granites are widespread along the LMB (Fig. 1b). Published chronological data have been used to interpret collisional and post-collisional magmatic events related to the closure of the Paleo-Tethys Ocean (Supplementary Table 1). Recent studies in the LMB report the presence of Triassic plutons at Leiwuqi (ca. 249–237 Ma; Wang et al., 2011; Hu et al., 2014), Jitang (ca. 223–214 Ma; Tao et al., 2014; Fan et al., 2019), Kagong (ca. 235–232 Ma, Wang et al., 2018c), Dongdashan (ca. 241–220 Ma, Yang et al., 2014; Peng et al., 2015), and Xiaochangdu (ca. 263–257 Ma, Wang et al., 2018c). The Lincang Batholith in the CSZ records a long-lived crustal magmatic event spanning the period ca. 239–203 Ma (Peng et al., 2006, 2013; Hennig et al., 2009; Kong et al., 2012; Nie et al., 2012; Dong et al., 2013; Wang et al., 2014c; Yang et al., 2014; Wang et al., 2015b; Deng et al., 2018; Zeng et al., 2018; Zhao et al., 2018a; Cong et al., 2020). The Late Triassic (ca. 239–229 Ma) volcanic units in Manghuai Formation at the Lincang Batholith have similar spatial and temporal relationships with the Biluo-xueshan Pluton (Peng et al., 2006, 2013; Wang et al., 2010; Wei et al., 2016; Cong et al., 2020). Furthermore, the Early to Middle Triassic (ca. 247–229 Ma) volcanic arc units included in the Cuiyibi Formation are exposed to the east of the Biluo-xueshan Pluton (Fan et al., 2014; Xu et al., 2016; Zhang et al., 2017; Xin et al., 2018; Yang et al., 2020).

As mentioned earlier, published U-Pb zircon dating from the LMB and CSZ provides significant constraints on understanding the evolution of the Paleo-Tethys Ocean (Supplementary Table 1). Yet, no precise U-Pb zircon dating has been published on the Biluo-xueshan Pluton, although a biotite $^{40}\text{Ar}/^{39}\text{Ar}$ date of ca. 222 Ma was documented of a sample from the pluton by Liu et al. (1999).

In this study, the high Th/U ratios and the well-defined oscillatory growth zoning in the zircons from the Biluo-xueshan Pluton indicate a magmatic origin (Hoskin and Schaltegger, 2003). The quartz diorite yields zircon U-Pb ages of 231 ± 1 Ma, indicating the earliest phase of emplacement of the Biluo-xueshan Pluton. Zircon U-Pb dates from the granodiorite (227 ± 1 Ma) and alkali-feldspar granite (227 ± 2 Ma) suggest that the pluton was emplaced mainly at ca. 227 Ma. Meanwhile, zircon U-Pb dates of other alkali-feldspar granite collected from northern and southern segments of the pluton have documented three late pulses with peaks at ca. 224, ca. 222, and ca. 217 Ma, respectively (Fig. 2a). Broad crystallization age span (ca. 14 million years) of the Biluo-xueshan Pluton recorded a long-lived crustal magmatic system which were comparable in magmatic duration of the Lincang Batholith. This ca. 231–217 Ma magmatism correlates with previous studies in the

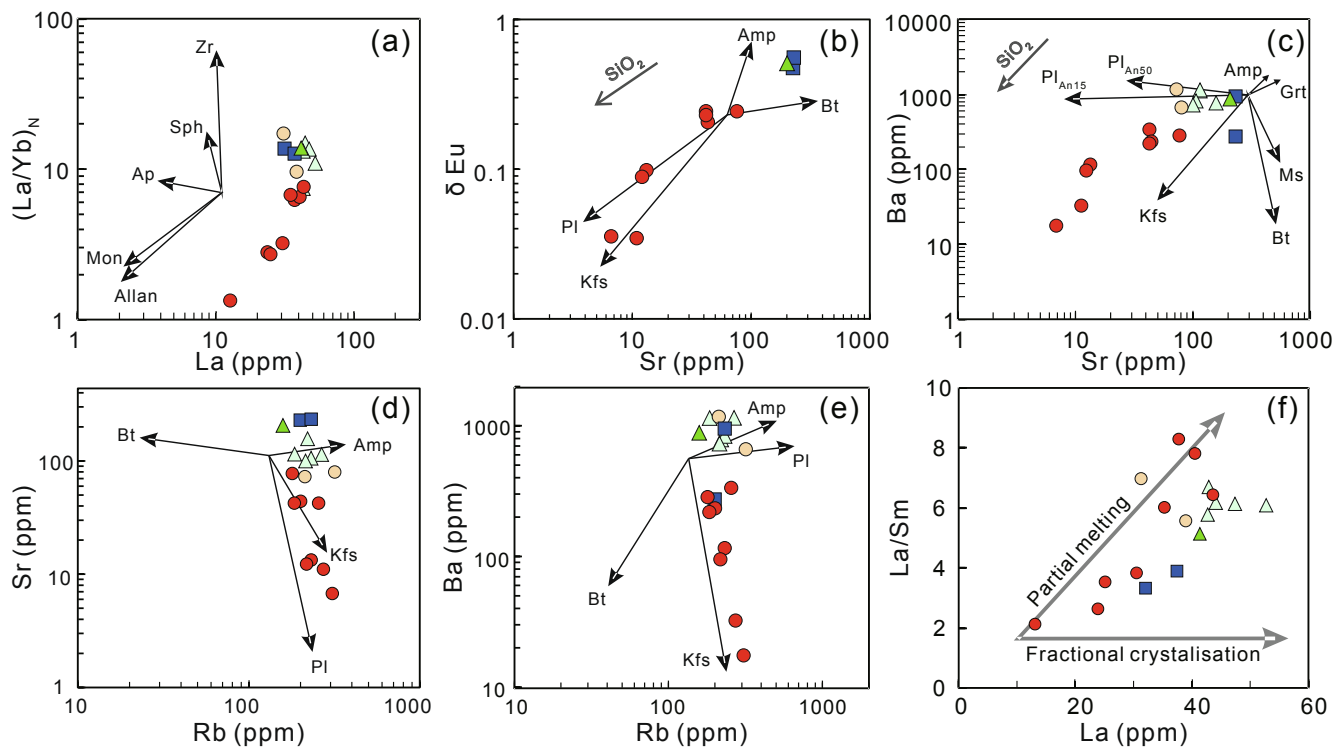


Fig. 11. Diagrams of fractional crystallisation simulation (after Rollinson, 1993; Sami et al., 2018) showing: (a) $(\text{La}/\text{Yb})_N$ vs La; (b) δEu vs Sr; (c) Ba vs Sr; (d) Sr vs Rb; (e) Ba vs Rb; and (f) La/Sm vs La. Abbreviations: Allan = allanite; Amp = amphibole; Ap = apatite; Bt = biotite; Grt = garnet; Kfs = K-feldspar; Mon = monazite; Ms = muscovite; Pl = plagioclase; Sph = sphene; Zr = zircon. Data sources and symbols are the same as for Fig. 8.

LMB and CSZ interpreted as representing post-collisional magmatism (Tao et al., 2014; Peng et al., 2015; Deng et al., 2018).

5.2. Petrogenesis of phases in the Biluoxueshan Pluton

5.2.1. Quartz diorite

The quartz diorite contains hornblende and allanite, and lacks garnet, muscovite, and cordierite (Fig. 4g), suggesting that their parental magma was hydrated and metaluminous. The quartz diorite is characterised by its low SiO_2 (58.30–60.47 wt%), $\text{Na}_2\text{O} + \text{K}_2\text{O}$ (5.93–6.98 wt%) and A/CNK (0.93–0.98) values, and high MgO (3.25–3.75), $\text{Mg}^\#$ (48–49), Cr (78–88 ppm), Ni (55–78 ppm), and V (139–141 ppm) contents (Fig. 7c, d, f). These values are typical of a mafic source (Rudnick and Gao, 2003; Du et al., 2018). Furthermore, the $\text{Mg}^\#$ values and Cr and Ni contents are much lower than those expected from mantle melts characterised by $\text{Mg}^\#$ values between 73 and 81, and contents of > 1000 ppm Cr and > 400 ppm Ni (Wilson, 2007). Explanations include fractional crystallisation of a parental magma and a mafic source within the crust (Du et al., 2018). The fractional crystallisation option is supported by the low differentiation index of 61–71 and the geochemical characteristics of the quartz diorite described earlier. In addition, the quartz diorites from the Biluoxueshan Pluton have low Sr contents between 230 and 234 ppm, depletion in HREEs with $(\text{Gd}/\text{Yb})_N$ values of 3.47–4.48, and an obvious Eu anomaly with δEu values between 0.48 and 0.57 (Fig. 9a), which are interpreted as being related to plagioclase and garnet fractionation (c.f. Patino Douce, 1996; Yuan et al., 2007). The negative Nb, Ta and Ti anomalies in the samples could also be due to the fractionation of Ti-bearing minerals (Fig. 9b), which are not characteristic of a N-MORB or OIB source. On the $(\text{La}/\text{Yb})_N$ vs La diagram in Fig. 11a, all the quartz diorites are subject to limited zircon and sphene fractionation. The La versus La/Sm diagram in Fig. 11f appears to show that the evolution of the magma

includes a partial melting process rather than fractional crystallisation.

The quartz diorites have variable Nb/Ta ratios of 13.9–18.9, which overlap the value of 17.5 ± 2 for magma derived from an enriched mantle (Kamber and Collerson, 2000), and the average value of 11–12 for the lower continental lower crust (Rudnick and Gao, 2003; Pfänder et al., 2007). The chemical composition of zircons in the quartz diorite includes high Th and U contents, a moderate Y content, and moderate U/Yb ratios (Fig. 13a, b), which are characteristic of zircons from the continental crust and similar to Mesozoic to Cenozoic zircons in the Lhasa Terrane (Liu et al., 2014; Zhu et al., 2017). Furthermore, the low Nb/La (0.39–0.75) and La/Ta (25–35) ratios are more like those from the lithospheric mantle rather than asthenospheric mantle (Karsli et al., 2020). The quartz diorites also have high CaO/Na₂O and low Al₂O₃/TiO₂ ratios that are characteristic of mafic (basalt-derived) sources (Sylvester, 1998; Fig. 14a, b). Accordingly, we propose that the quartz diorites documented in this contribution originated from the partial melting of basalt-derived melt modified by the lithospheric mantle at a shallow depth (≤ 5 kbar; Fig. 14d–f).

5.2.2. Granodiorite

The geochemistry of the granodiorite in the Biluoxueshan Pluton presented in this contribution and by Luo et al. (2016) contains low contents of MgO, CaO, and Na₂O + K₂O, high A/CNK values of 1.15 to 1.26, K₂O/Na₂O values of 1.3 to 2.1, and normative-CIPW corundum contents of 1.1 to 3.4, which are consistent with the characteristics of S-type granites, but the presence of hornblende and lack of aluminium-rich minerals such as garnet, cordierite and muscovite, are characteristics of I-type granites (Chappell, 1999; Chappell and White, 1974, 2001; Clemens, 2003). All the granodiorites are characterised by low Na₂O + K₂O – CaO (2.55–4.78 wt%) contents and FeO_T/MgO (1.7–2.4) values, and plot in the magnesian field in Fig. 7e, which are values lower than those of typical A-type granites (Frost and Frost, 2011). The parent

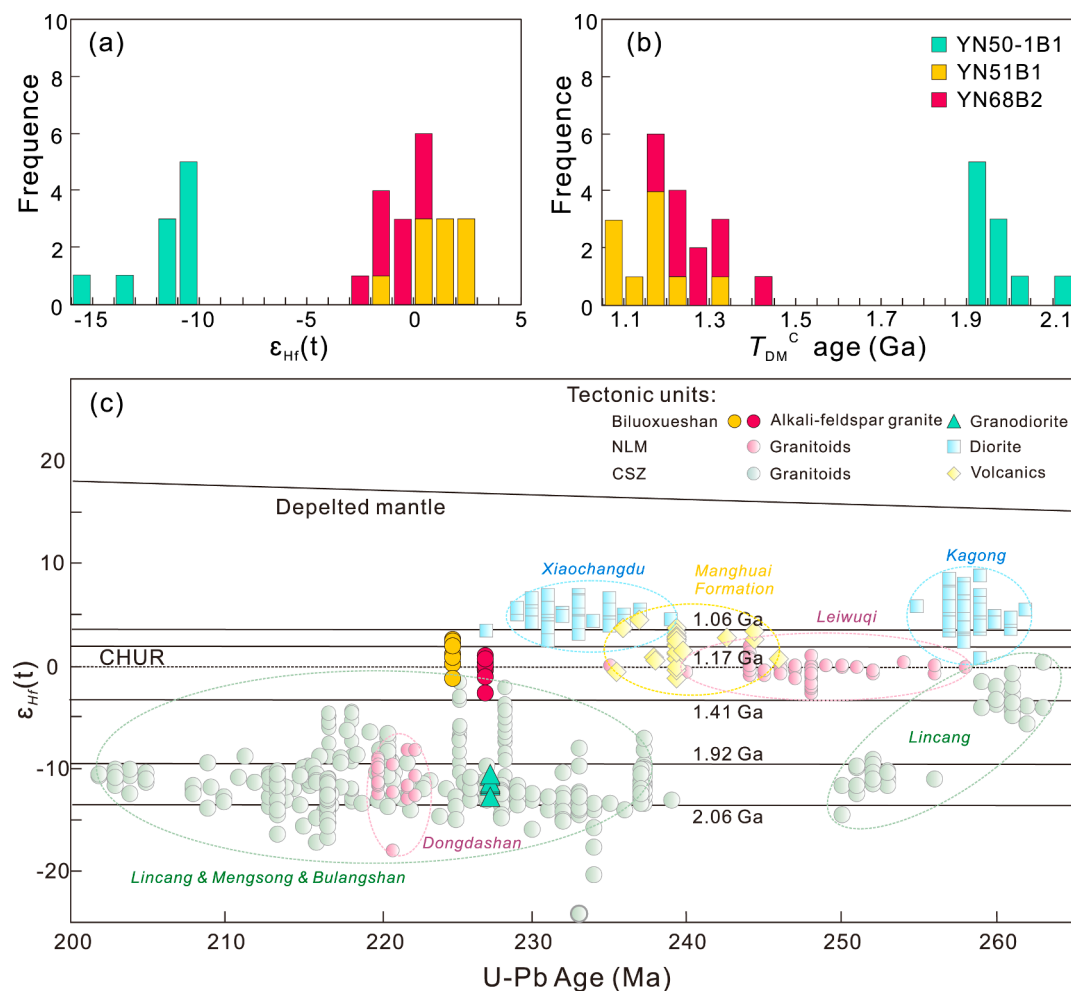


Fig. 12. Histograms for samples from the Biluoqeshan Pluton showing: (a) $\epsilon_{Hf}(t)$ isotope data for the granodiorite and alkali-feldspar granite; (b) Hf model ages for the granodiorite and alkali-feldspar granite; and (c) $\epsilon_{Hf}(t)$ values vs U-Pb crystallisation ages diagrams for zircons from the igneous rocks. The Hf isotopic data for the northern LMB and CSZ are from publications cited in Supplementary Table 1.

magma for the granodiorite appears to have undergone limited fractional crystallisation, as shown from the fractional crystallisation diagram in Fig. 11 and its low differentiation index value of 55.7. The granodiorite is peraluminous and has a calc-alkaline affinity with a significantly negative Eu anomaly, is depleted in Ba, Nb, Sr and Ti, and enrichment in Rb, Th, U and Pb (Fig. 9a, b). These characteristics are typical of crustal melts (Miller, 1985; Harris et al., 1986; Deng et al., 2018).

The granodiorite yields negative zircon $\epsilon_{Hf}(t)$ values between -13 and -10.8, corresponding to Hf crustal model ages of 2060 to 1920 Ma showing that the source is Palaeoproterozoic in age (Fig. 12c). Palaeoproterozoic model ages have also been documented for the Late Triassic Jitang and Dongdashan plutons in the LMB, and the Lincang, Mengsong and Bulangshan plutons in the CSZ (Dong et al., 2013; Tao et al., 2014; Peng et al., 2015; Wang et al., 2015b; Deng et al., 2018; Cong et al., 2020). Furthermore, most of zircons from the granodiorite have moderate Th and U contents with Th/U ratios of 0.17–0.82, and are typical of zircons derived from the continental crust (Fig. 13a, b).

In the absence of mineral fractionation, peraluminous melts originating from part-melts of meta-igneous rocks should have high Na contents, low HREE contents, high Al concentrations with residues of garnet-cordierite-muscovite, and significant depletion in LILEs, U and Th (Petford and Atherton, 1996; Clemens, 2003). The granodiorite does not display such geochemical signatures, but the presence of hornblende

is characteristic of an igneous source (Chappell and White, 1974). In addition, all granodiorites have higher CaO/Na₂O ratios of 0.85–1.17, and lower Al₂O₃/TiO₂ ratios of 14.7–23.7 and Rb contents of 158–266 ppm relative to pelite-derived melts, indicating that their parental magma was not the product of partial melting of a metasedimentary source (Miller, 1985; Sylvester, 1998; Peng et al., 2015). On the Rb/Ba vs Rb/Sr diagram in Fig. 14c, the granodiorite plots in the clay-poor field close to the shale and psammite field. Therefore, the major element signatures and zircon Hf isotopic compositions indicate that the granodiorite has a mixed meta-igneous and metasedimentary source (Miller, 1985; Holtz and Johannes, 1991; Clemens, 2003), or mineral fractionation did happen in the parental magma. In addition, given that the Hf crustal model age for the granodiorite is 2060–1920 Ma, the source is Palaeoproterozoic in age and derived from the middle to upper crust.

5.2.3. Alkali-feldspar granite

The mineralogical of the alkali-feldspar granite is characterised by perthite and interstitial biotite, the absence of aluminium-rich minerals (such as garnet, cordierite, and muscovite), and its low CIPW normative corundum value of 0.2–1.1. As described above, the alkali-feldspar granites are characterised by relatively high SiO₂ and Na₂O + K₂O contents and K₂O/Na₂O ratios, low Al₂O₃, CaO, MgO, and P₂O₅ contents, and are metaluminous to weakly peralkaline (Fig. 7c). These characteristics are consistent with SiO₂ enrichment due of crystal

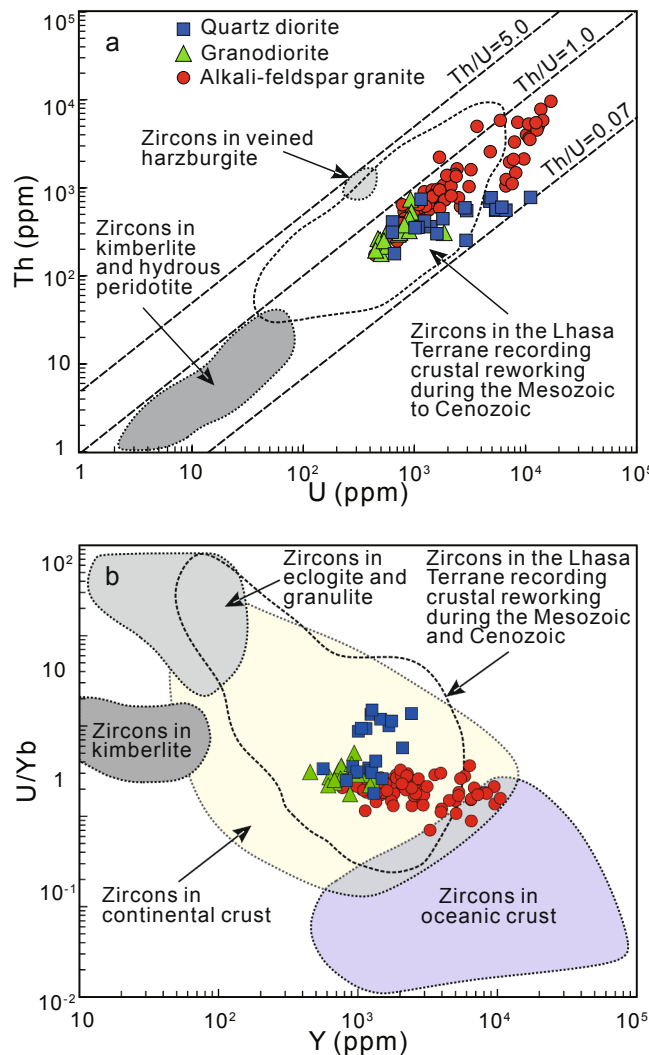


Fig. 13. Discriminant diagrams for zircons from the quartz diorite, granodiorite, and alkali-feldspar granite sampled from the Biluoqueshan Pluton showing: (a) Th vs U plot (after Liu et al., 2014); and (b) U/Yb vs Y (after Grimes et al., 2007).

fractionation (c.f. Bowen, 1928; Clemens, 2003; Bonin, 2007; Fig. 7e, f).

The validity of common discrimination diagrams is challenged by depletion in Zr (<200 ppm), which is typical of crystal fractionation (Whalen et al., 1987; Lee and Bachmann, 2014). Samples of alkali-feldspar granite have moderately high Zr + Nb + Ce + Y contents (Fig. 10a, b), and plot at or near the boundary between the I-S-M-type, fractionated, and A-type granites (Fig. 10c, d). The samples are positively anomalous in Rb, Th, U, K, Nd, Zr, and Hf, and negatively anomalous in Ba, Sr, P, Ti, and Eu with “seagull-type” REE patterns (Fig. 9e), like those of A-type granites (Collins et al., 1982; Whalen et al., 1987; Wu et al., 2002). Additionally, the calculated zircon saturation temperatures (T_{Zr}) for the alkali-feldspar granites vary from 742 to 823 °C, being the minimum initial magma temperature at the source (Watson and Harrison, 1983). However, the relatively low temperatures yielded by the alkali-feldspar granites may record oxidising magmatic conditions and high-water concentrations (Miller et al., 2003; Jiang et al., 2018). Therefore, the alkali-feldspar granites described in this study from the Biluoqueshan Pluton are fractionated granites plotting between the I-, S-, M- and A-type granites (Fig. 10a–d).

The significantly high SiO₂ contents of 75.57–77.06 wt% and high differentiation indexes (DI) of 93.1–96.4 for the alkali-feldspar granites further support the interpretation that they are highly fractionated

(Fig. 10e–f). The petrogenesis of such highly fractionated granites are difficult to ascertain and tend to exhibit similar petrography and geochemistry as haplogranites (King et al., 1997; Li et al., 2007; Wu et al., 2007, 2017). The Harker diagrams in Fig. 8 show that the Fe₂O₃, MgO, P₂O₅, and TiO₂ contents are inversely proportional to SiO₂, which are consistent with the fractionation of hornblende, biotite, apatite, and Fe-Ti oxides from a magma. The K₂O contents is directly proportional with the SiO₂ (Fig. 7d), which is characterised by the cumulation of megacrystic K-feldspar in the samples (Fig. 4h, i). The prominently negative Eu and Sr anomalies are indicative of significant plagioclase fractionation (Fig. 9a), and the Ba negative anomalies are associated with the fractionation of K-feldspar (Hanson, 1978). The negative P anomaly indicates the fractionation of apatite, and the prominent negative Nb, Ta, and Ti anomalies are commonly attributed to the fractionation of Ti-bearing minerals, such as ilmenite and titanite (Fig. 9b; Rollinson, 1993). Furthermore, the variation of the alkali-feldspar granite’s REE pattern in the (La/Yb)_N vs La diagram shown in Fig. 11a appears to be related to the fractionation of allanite and monazite. The positive correlation in the Sr vs δEu and Sr vs Ba plots and the Rb vs Sr and Rb vs Ba plots show that significant fractional crystallisation of plagioclase took place in the parental magma (Fig. 11b–e). These observations are consistent with the petrological observations of

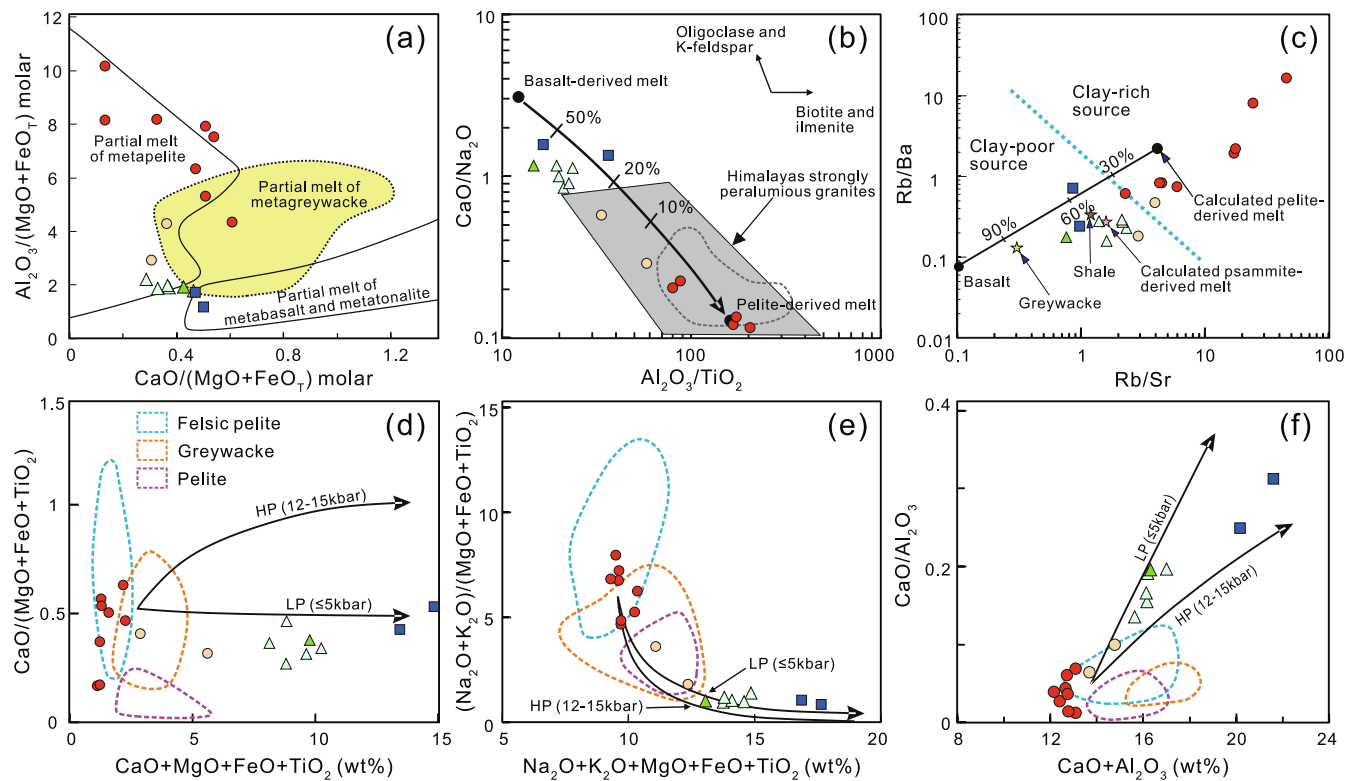


Fig. 14. Discrimination diagrams for the sources for samples from the Biluoqueshan Pluton: (a) molar $\text{CaO}/(\text{MgO} + \text{FeO}_T)$ vs molar $\text{Al}_2\text{O}_3/(\text{MgO} + \text{FeO}_T)$ plot (after Altherr et al., 2000); (b) $\text{Al}_2\text{O}_3/\text{TiO}_2$ vs $\text{CaO}/\text{Na}_2\text{O}$ plot (after Sylvester, 1998); (c) Rb/Sr vs Rb/Ba plot (after Janoušek et al., 2004); and (d)–(f) compositions of the samples from the Biluoqueshan Pluton compared to compositional ranges of experimental metasediment-derived melts of greywacke, felsic and mafic pelite (after Patiño Douce, 1999). The two thick solid lines are reaction curves that model compositions of melt produced by hybridisation of high-Al olivine tholeiite with metagreywacke at low pressures (LP, $P \leq 5$ kbar) and high pressures (HP, $P = 12$ – 15 kbar) (after Patiño Douce, 1999). Symbols are the same as in Fig. 8.

the alkali-feldspar granites, which have abundant K-feldspar megacrysts and minor amounts of plagioclase and biotite.

The La vs La/Sm plot in Fig. 11f indicates that the parental magma of the phases in the Biluoqueshan Pluton were generated by partial melting of their source. However, single-stage partial melting could not have produced a pluton with very low Sr (< 78 ppm) and high Rb (> 179 ppm) contents, especially when feldspar has fractionated from highly evolved granites (e.g. Halliday et al., 1991; Sami et al., 2018). Therefore, we propose that partial melting was followed by extensive fractional crystallisation in a closed system, which would explain the geochemistry of the analyses phases of the Biluoqueshan Pluton (c.f. Sami et al., 2018).

Up to now, highly fractionated A-type granites associated with an extensional tectonic setting have been interpreted as: (1) extreme differentiation of mantle-derived magma (e.g. depleted mantle, or alkaline basic magmas; Bonin, 2007; Mao et al., 2014); (2) partial melts of various types of crustal material (Whalen et al., 1987; King et al., 1997; Bonin, 2007; Huang et al., 2011); and (3) melts of combined crustal and mantle sources (Kemp et al., 2005; Bonin, 2007). It has been proposed that the extensive fractional crystallisation of mantle-derived magma from mafic through intermediate to felsic compositions requires the presence of abundant mafic, intermediate, and lesser felsic rocks (Wu et al., 2002). Neither mafic micro-granular enclaves nor large volumes of coeval mafic rocks have been found near or in the alkali-feldspar granites. We, therefore, exclude the involvement of magmatic differentiation in the mantle for the petrogenesis of the alkali-feldspar granite.

Peralkaline A-type granites in the Lachlan Fold Belt of SE Australia are believed to be related to the fractionation of mafic magmas (King et al., 1997). In this study, however, the high SiO_2 and alkaline ($\text{Na}_2\text{O} + \text{K}_2\text{O}$) contents, and low MgO , Ni , and Cr contents of the alkali-feldspar granites indicate they have a crustal source, rather than being directly generated by partial melting of a mafic source in the mantle. The Nb/Ta

ratios of 10.9–14.4 for the alkali-feldspar granites are also consistent with derivation from the continental crust, which has a Nb/Ta ratio of 11–12 (Rudnick and Gao, 2003; Pfänder et al., 2007). Furthermore, the zircon chemical compositions of the samples have high Th and U contents, and moderate Th/Yb ratios and Y contents (Fig. 13a, b), also characteristic of zircons derived from the continental crust (Liu et al., 2014).

Generally, Hf isotope ratios of zircons are rarely affected by later geological events once the Hf system has closed, making this signature an effective tool in deciphering the crustal tectonic setting and tracing the source of the parentally magma of a granite (Wu et al., 2007; Kröner et al., 2012). Two samples of the alkali-feldspar granite have zircon $\varepsilon_{\text{Hf}}(t)$ values of -1.3 to $+2.6$ (corresponding to T_{DM}^{C} ages of 1310–1060 Ma), and -2.7 to $+1$ (corresponding to T_{DM}^{C} ages of 1410–1170 Ma). These data are distinct from those of the Late Triassic plutons with a crustal source, such as the Lincang, Dongdashan, Mengsong and Bulangshan batholiths (Fig. 12c), but like the rhyolite in the Late Triassic Manghuai Formation that has a Mesoproterozoic source (Yang et al., 2014; Cong et al., 2020). The source for the alkali-feldspar granite shown in Fig. 12 is between juvenile and reworked older source material with a signature close to Chondritic Uniform Reservoir (CHUR) values. These observations are interpreted in terms of A-type granites generated by the partial melting of the Mesoproterozoic juvenile crust (Fig. 12c).

High-potassium calc-alkaline magmas are interpreted as originating from: (1) mantle-derived K-rich magmas (Roberts and Clemens, 1993; Sisson et al., 2005); or (2) mixed mantle-derived and crustal partial melts (Ferré and Bernard, 2001; Karsli et al., 2007; Topuz et al., 2019). The second option involving mixed mantle and crustal derived melts is considered a plausible mechanism for generating the high-K alkali-feldspar granites in the Biluoqueshan Pluton.

It has been proposed, from experimental petrology studies, that

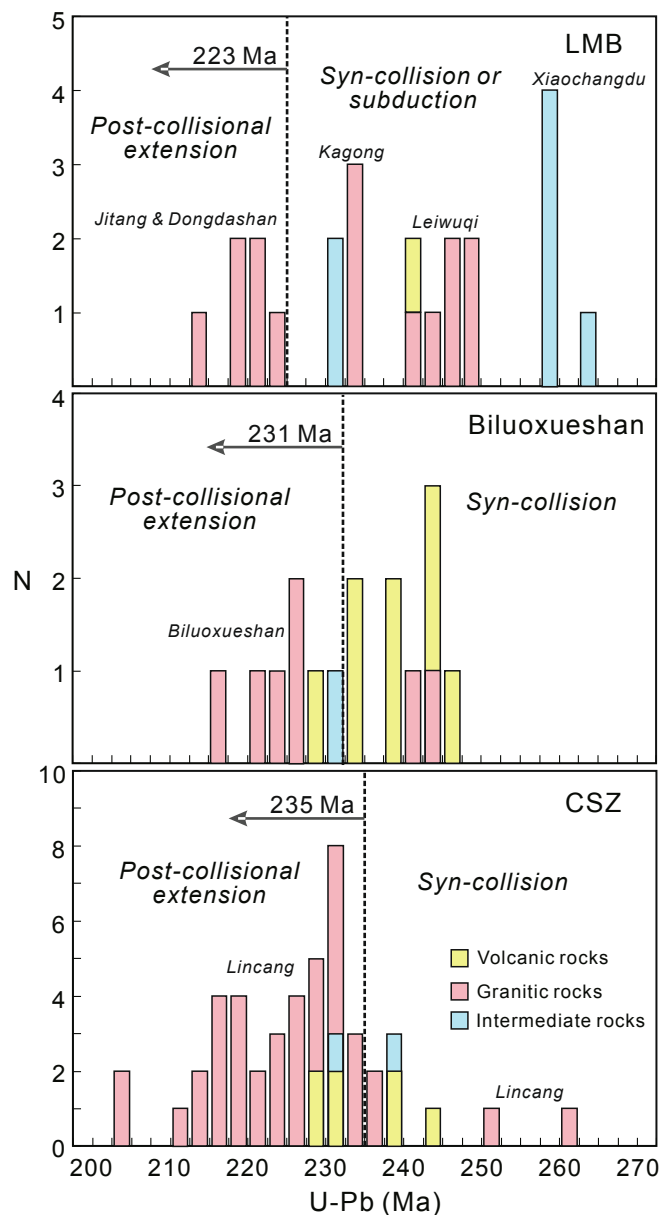


Fig. 15. Zircon U-Pb age frequency distributions for Middle Permian to Late Triassic igneous rocks in the northern LMB, Biluoqueshan Pluton and surrounding area, and CSZ. Data sources are listed in Supplementary Table 1.

highly fractionated aluminous A-type granitic magmas could be generated from partial melts of tonalite and granodiorite at high temperatures and low pressures of around 4 kbar (Creaser et al., 1991; King et al., 1997; Patiño Douce, 1997, 1999). The composition of the alkali-feldspar granites is consistent with the modelling reaction curves at low pressures of ≤ 5 kbar, supporting the conclusion that its source is the middle to upper crust (Fig. 14d–f).

5.3. Tectonic setting

There is commonly thought that the tectonic history of the Paleo-Tethys Ocean included Permian to Triassic magmatism in the CSZ related to the subduction of oceanic plate followed by crustal collision, and crustal thickening followed by extensional tectonics or gravitational collapse (Yang et al., 2014; Wang et al., 2015b). Although it is proposed that the LSZ and CSZ formed a continuous belt where the Paleo-Tethys Ocean closed (Wang et al., 2015b; Deng et al., 2018), there are still

gaps in our understanding of the tectonic evolution of the Biluoqueshan Pluton. Luo et al. (2016) suggest that the different phases in the pluton formed in a late syn- to post-collisional setting, but lack geochronological evidence for this hypothesis.

Several Late Permian to Late Triassic volcanic units are identified as being laid down during the transition from a continental arc-setting to a syn-collisional volcanic setting (Fan et al., 2014; Yang et al., 2014; Zhang et al., 2017; Yang et al., 2020). The continental arc-volcaniclastics are folded in a northerly direction parallel to the orientation of the Biluoqueshan pluton, which is consistent with compression perpendicular to the orogen and after the volcanism (Yang et al., 2014).

The common absence of Early Triassic sedimentary units in the Biluoqueshan area are consistent with uplift and erosion at that time (YNBGMR, 1990; Zhong, 1998; Peng et al., 2006, 2013). Late Early- to Middle-Triassic andesite and rhyolite-dacite volcanic rocks are intercalated with purple-red and minor grey shale in the area, which are unconformably overlain by Early Jurassic units (YNBGMR, 1990; Yang et al.,

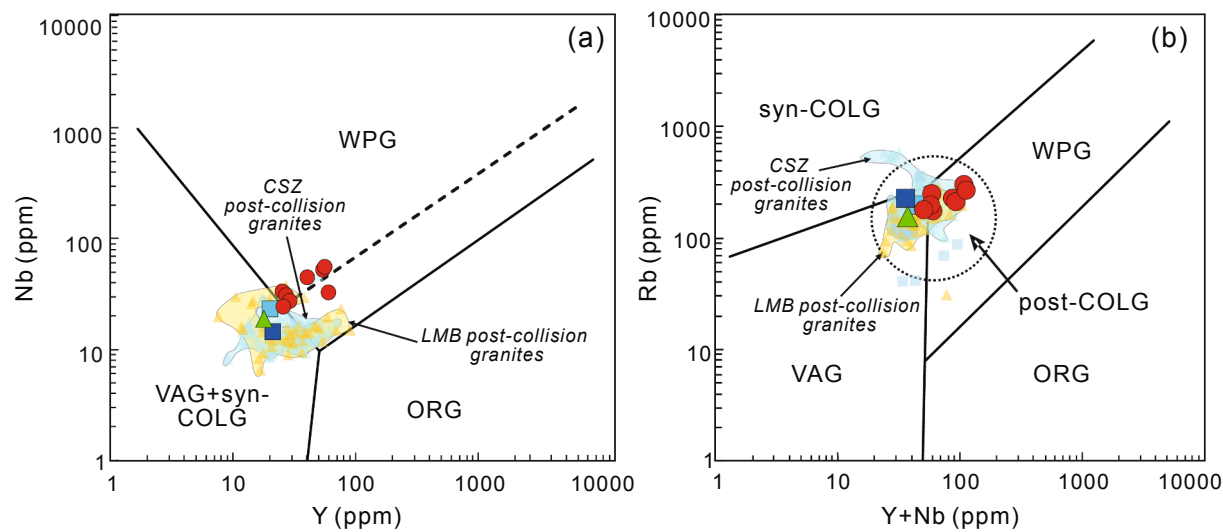


Fig. 16. Discrimination diagrams: (a) Nb vs Y plot (after Pearce et al., 1984); and (b) Rb vs ($Y + Nb$) discrimination plot (after Pearce, 1996). Abbreviations: VAG = volcanic arc granites, Syn-COLG = syn-collision granites, Post-COLG = post-collision granites, WPG = within plate granites, and ORG = ocean-ridge granites. Symbols and data sources are the same as in Fig. 7.

2014). This was followed by Late Triassic mafic and felsic volcanism, with little or no intermediate compositions. Examples are the basalt in the Xiaodingxi Formation and rhyolite in the Manghuai Formation, which are typical rock types associated with extensional tectonics (e.g. Brewer et al., 2004). The stratigraphic contacts show that the Late Triassic rocks are likely to have been formed in a post-collisional tectonic setting, similar to the coeval Lincang Batholith (Peng et al., 2013; Wang et al., 2015b; Deng et al., 2018; Fig. 3).

As discussed above, the multiple phases in the Biluoqueshan Pluton yield U-Pb zircon dates of ca. 231–217 Ma coeval with post-collisional magmatism following the closure of the Paleo-Tethys Ocean in the CSZ (ca. 235–203 Ma) and LMB (ca. 223–214 Ma) (Fig. 15). Hence, the development of the Biluoqueshan Pluton relates to orogenic process following the closure of the Paleo-Tethys Ocean.

High-K calc-alkaline plutons, especially alkaline and A-type granites, relate to post-collisional settings marking the waning stage of an orogenic event (Sylvester, 1989; Liegeois et al., 1998; Kemp et al., 2005; Bonin et al., 2007; Tian et al., 2018). The Late Triassic alkali-feldspar granites in the Biluoqueshan Pluton and coeval volcanic units in the Manghuai Formation have geochemical similarities, indicating that they formed in the same post-collisional extensional setting related to the waning stage of an orogeny, which we name here the Biluoqueshan Orogen (new name).

Broadly speaking, the tectonic settings for the development of magmas include crustal thickening associated with gravitational collapse or transpressional deformation, and crustal thinning resulting from the development of a back-arc basin during the subduction of oceanic crust of post-collisional rifting (c.f. Stampfli and Borel, 2002; Peng et al., 2013, 2015). The petrogenesis of the plutonic rocks sampled in our study straddle the volcanic-arc, syn-collisional and within-plate granitic fields on the Nb vs Y and Rb vs $Y + Nb$ diagrams (Fig. 16a, b) which, with the Late Triassic post-collisional granites in CSZ and LMB, points towards magma developing during a post-collisional extensional setting between ca. 231 and 217 Ma (c.f. Pearce, 1996).

5.4. Implication for the evolution of the Paleo-Tethyan Ocean

Diverse tectonic models have been proposed for post-collisional extension in the CSZ. A common hypothesis is that the Late Triassic magmatism is related to slab break-off, even though there has been no explanation as to how a slab of relatively lower density can sink into the mantle with a higher density (c.f. Peng et al., 2013, 2015; Wang et al.,

2015b). Considering the data documented here and available in the literature, Fig. 17 presents a model illustrating the evolution of the Biluoqueshan Pluton, which is discussed below.

Volcanism associated with subduction and collisional tectonics, such as in the Cuiyibi Formation (Fig. 2a), took place during the ca. 247–231 Ma Biluoqueshan Orogeny (Fan et al., 2014; Xu et al., 2016; Zhang et al., 2017; Xin et al., 2018; Yang et al., 2020). Major northward-trending extensional structures parallel to or subparallel with the CSZ developed or were reactivated during or shortly after the waning stages of the orogeny. These crustal structures controlled the emplacement of the Late Triassic Biluoqueshan, Lincang, Dongdashan, and Jitang batholiths (c.f. Peng et al., 2006, 2013; Hennig et al., 2009; Wang et al., 2015b).

The HP Chongshan Metamorphic Complex is located west of the CSZ orientated parallel with the long axis of the Biluoqueshan Pluton. The western boundary of the complex potentially marks the location of a subduction zone in the Paleo-Tethys Ocean (c.f. Davies and von Blanckenburg, 1995). It is along such a crustal zone of weakness that can be reactivated as a rift where large volumes of magma would be emplaced during the Late Triassic (Bonin, 2004). Similar controls are envisaged for the emplacement of Late Triassic granitic belts in other parts of the Sanjiang Orogen, such as at the Lincang, Dongdashan, and Jitang batholiths.

The intrusion of the hot asthenospheric mantle into a narrow lithospheric gap above the subducted slab can generate a thermal anomaly in the mantle wedge. Such a thermal anomaly will cause partial melting of an overlying enriched mantle wedge and lower continental crust, inducing magmatism in the crust (Davies and von Blanckenburg, 1995; Ma et al., 2015). With this scenario, the Biluoqueshan A-type granites would be attributed to underplating of mantle-derived or juvenile lower crust-derived magma at shallow depths during extensional events, inducing partial melting of felsic crustal rocks (Fig. 17a).

From the detailed geochronological data available, post-collisional granites were emplaced during the Triassic starting at ca. 235 Ma (Wang et al., 2015b; Deng et al., 2018), continuing at ca. 231 Ma in the Biluoqueshan Pluton (this study), and ca. 223 Ma in the LMB (Tao et al., 2014; Peng et al., 2015; Fan et al., 2019). Assuming these data are correct, this shows a gradually progression in the CSZ towards the northeast (Fig. 15). Therefore, our new data show that the closure of the Paleo-Tethys Ocean was near the Lincang Batholith in the south and progressed northward, resulting in a scissor-like fashion (Fig. 17b), followed by collisional tectonics, and finally a post-collisional extension at ca. 235 Ma in the south and at ca. 223 Ma in the north between the

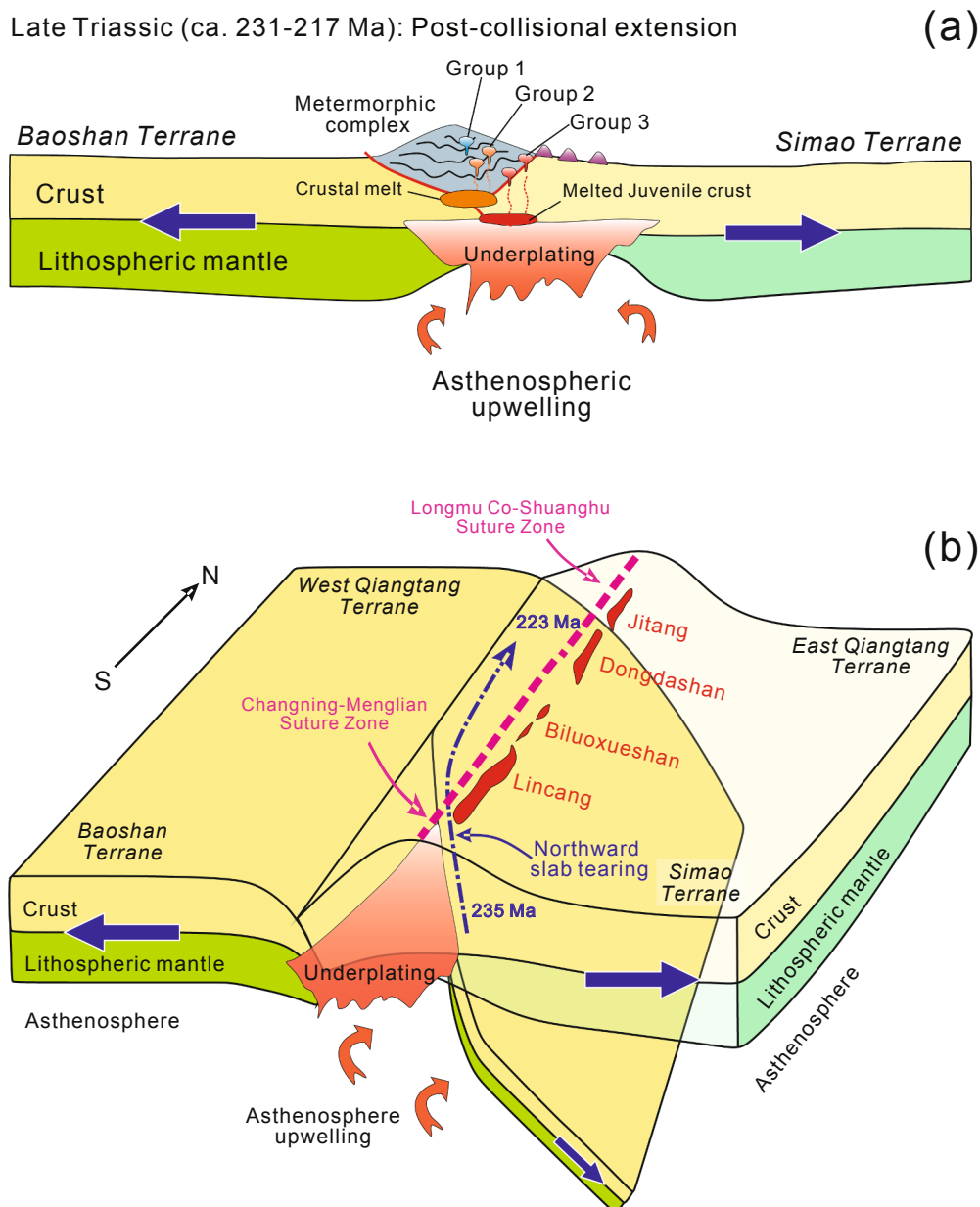


Fig. 17. Schematic model showing the geodynamic evolution of the Sanjiang Orogen: (a) upwelling of mantle-derived melts in an extensional setting for the emplacement Late Triassic granitic and rhyolitic magmatism; (b) a Late Triassic northward scissor-like fashion for the post-collisional extension took place from ca. 235 to 223 Ma in the Changning-Menglian Suture Zone between the Baoshan and Simao terranes.

Baoshan and Simao terranes.

6. Conclusions

Zircon U-Pb dating of multiple phases in the Biluoqueshan Pluton yields crystallisation ages 231 ± 1 Ma for quartz diorite, 227 ± 1 Ma for granodiorite, and ca. 227–217 Ma for alkali-feldspar granites. The petrological and geochemical of these granitoids indicate that quartz diorites are derived from partial melting of a mafic source in the crust that were modified by the lithospheric mantle, and granodiorites have a partially melted Palaeoproterozoic source in the crust. Alkali-feldspar granites are highly fractionated and have an A-type affinity with a source generated by the partial melting of Mesoproterozoic juvenile crustal with a mantle-derived component.

The Late Triassic magmatism in the Changning-Menglian Suture Zone took place in a post-collision tectonic setting. It is proposed that the

emplacement of the Late Triassic plutons progressed northwards resulting in a younging direction from south to the north. This scissor-like configuration related to a northward-propagating post-collisional extension during ca. 235–223 Ma between the Baoshan and Simao terranes in the Changning-Menglian Suture Zone.

CRediT authorship contribution statement

Qi Chen: Conceptualization, Methodology, Writing - original draft. **Changming Wang:** Supervision, Funding acquisition. **Leon Bagas:** Supervision, Writing - review & editing. **Bin Du:** Investigation. **Kangxing Shi:** Investigation. **Lifei Yang:** Investigation. **Jiaxuan Zhu:** Investigation. **Hongyu Duan:** Investigation.

Declaration of Competing Interest

The authors declare that they have no known competing financial interests or personal relationships that could have appeared to influence the work reported in this paper.

Acknowledgements

This work was supported by the National Key Research and Development Project of China (Number 2020YFA0714802), National Natural Science Foundation of China (Numbers 41872080), and Most Special Fund from the State Key Laboratory of Geological Processes and Mineral Resources in China University of Geosciences (Beijing) of China (Number MSFGPMR201804). We are grateful to State Key Laboratory of Continental Dynamics in Northwestern University (Xi'an), State Key Laboratory of Geological Processes and Mineral Resources of China University of Geosciences in Wuhan, and National Research Center of Geoanalysis in Beijing for their help with zircon U-Pb and Lu-Hf isotope and whole-rock geochemistry analysis.

Appendix A. Supplementary material

Supplementary data to this article can be found online at <https://doi.org/10.1016/j.jseas.2021.104700>.

References

- Altherr, R., Holl, A., Hegner, E., Langer, C., Kreuzer, H., 2000. High-potassium, calc-alkaline I-type plutonism in the European Variscides: northern Vosges (France) and northern Schwarzwald (Germany). *Lithos* 50, 51–73.
- Andersen, T., 2002. Correction of common lead in U-Pb analyses that do not report ^{204}Pb . *Chem. Geol.* 192, 59–79.
- Bonin, B., 2004. Do coeval mafic and felsic magmas in post-collisional to within-plate regimes necessarily imply two contrasting, mantle and crustal, sources? A review. *Lithos* 78, 1–24.
- Bonin, B., 2007. A-type granites and related rocks: Evolution of a concept, problems and prospects. *Lithos* 97, 1–29.
- Bowen, N.L., 1928. The evolution of the igneous rocks. Princeton University Press, Princeton, New Jersey, p. 332.
- Brewer, T.S., Åhäll, K.-L., Menegue, J.F., Storey, C.D., Parrish, R.R., 2004. Mesoproterozoic bimodal volcanism in SW Norway, evidence for recurring pre-Sveconorwegian continental margin tectonism. *Precambrian Res.* 134, 249–273.
- Chappell, B.W., 1999. Aluminium saturation in I- and S-type granites and the characterization of fractionated haplogranites. *Lithos* 46, 535–551.
- Chappell, B.W., White, A.J.R., 1974. Two contrasting granite type. *Pac. Geol.* 8, 173–174.
- Chappell, B.W., White, A.J.R., 2001. Two contrasting granite types: 25 years later. *Aust. J. Earth Sci.* 48, 489–499.
- Chen, Q., Wang, C.M., Du, B., He, Z.C., Zhu, J.X., Yang, L.F., Shi, K.X., 2019. Zircon LA-ICP-MS U-Pb dating and geochemistry of the Jitang metamorphic complex in eastern Tibet and their geological implications. *Acta Petrologica Sinica* 35, 1423–1446 (in Chinese with English abstract).
- Clemens, J.D., 2003. S-type granitic magmas-petrogenetic issues, models and evidence. *Earth-Sci. Rev.* 61, 1–18.
- Cohen, K.M., Finney, S.C., Gibbard, P.L., Fan, J.X., 2013. The ICS international chronostratigraphic chart. *Episodes* 36, 199–204.
- Collins, W.J., Beams, S.D., White, A.J.R., Chappell, B.W., 1982. Nature and origin of A-type granites with particular reference to southeastern Australia. *Contrib. Miner. Petrol.* 80, 189–200.
- Cong, B.L., Wu, G.Y., Zhang, Q., Zhai, M.G., Zhao, D.S., Zhang, W.H., 1993. PetroTECTONIC evolution of the Tethys zone in the western Yunnan, China. *Sci. China (Ser. B)* 23, 1201–1207 (in Chinese with English abstract).
- Cong, F., Wu, F.Y., Li, W.C., Mou, C.L., Huang, X.M., Wang, B.D., Hu, F.Y., Peng, Z.M., 2020. Origin of the Triassic Lincang granites in the southeastern Tibetan Plateau: Crystallization from crystal mush. *Lithos* 360–361, 105452.
- Creaser, R.A., Price, R.C., Wormald, R.J., 1991. A-type granites revisited: assessment of a residual-source model. *Geology* 19, 163–166.
- Davies, J.H., von Blanckenburg, F., 1995. Slab breakoff: A model of lithosphere detachment and its test in the magmatism and deformation of collisional orogens. *Earth Planet. Sci. Lett.* 129, 85–102.
- De la Roche, H., Leterrier, J., Grande Claude, P., Marchal, M., 1980. A classification of volcanic and plutonic rocks using R1-R2 diagrams and major element analyses-its relationship and current nomenclature. *Chem. Geol.* 29, 183–210.
- Deng, J., Wang, C.M., Bagas, L., Selvaraja, V., Jeond, H., Wu, B., Yang, L.F., 2017. Insights into ore genesis of the Jinding Zn-Pb deposit, Yunnan Province, China: Evidence from Zn and in-situ S isotopes. *Ore Geol. Rev.* 90, 943–957.
- Deng, J., Wang, C.M., Li, G.J., 2012. Style and process of the superimposed mineralization in the Sanjiang Tethys. *Acta Petrologica Sinica* 28, 1349–1361 (in Chinese with English abstract).
- Deng, J., Wang, C.M., Li, G.J., Zhou, D.Q., 2019. The theory of composite metallogenetic system: Key of recovering metallogenetic mystery in the SW Tethys. *Acta Petrologica Sinica* 35, 1303–1323 (in Chinese with English abstract).
- Deng, J., Wang, C.M., Zi, J.W., Xia, R., Li, Q., 2018. Constraining subduction-collision processes of the Paleo-Tethys along the Changning-Menglian suture: New zircon U-Pb ages and Sr-Nd-Pb-Hf-O isotopes of the Lincang batholith. *Gondwana Res.* 62, 75–92.
- Dong, G.C., Mo, X.X., Zhao, Z.D., Zhu, D.C., Goodman, R., Kong, H.L., Wang, S., 2013. Zircon U-Pb dating and the petrological and geochemical constraints on Lincang granite in Western Yunnan, China: implications for the closure of the Paleo-Tethys Ocean. *J. Asian Earth Sci.* 62, 282–294.
- Du, B., Wang, C.M., Yang, L.F., Shi, K.X., Chen, Q., Zhu, J.X., 2019. Petrogenesis of the Cenozoic Lianhuashan pluton (SW China): Constrained by zircon U-Pb geochronology, Lu-Hf isotope and geochemistry. *Geol. J.* 55, 3377–3400.
- Du, L., Long, X.P., Yuan, C., Zhang, Y.Y., Huang, Z.Y., Sun, M., Xiao, W.J., 2018. Petrogenesis of Late Paleozoic diorites and A-type granites in the central Eastern Tianshan, NW China: Response to post-collisional extension triggered by slab breakoff. *Lithos* 318–319, 47–59.
- Fan, B.L., Zhang, X.L., Yu, T., Bai, T., Feng, D.X., 2019. The genesis of Jitang duplex granites in east Tibet: Evidence from the zircon U-Pb age and rock geochemistry. *Geol. Bull. China* 38, 1274–1286 (in Chinese with English Abstract).
- Fan, H.P., Li, B., Zhou, J.X., Du, L.J., Sun, H.R., Huang, Z.L., Wu, T., 2020. Subduction-modified mantle-derived Triassic high-Mg andesites in the Sanjiang Tethys, eastern Tibet. *J. Asian Earth Sci.* 191, 104216.
- Fan, J.W., Yang, T.N., Liang, M.J., Shi, P.L., 2014. LA-ICP-MS zircon U-Pb geochronology and geochemistry of volcanic rocks on the western margin of Lanping Basin in western Yunnan and their tectonic implications. *Acta Petrologica et Mineralogica* 33, 471–490 (in Chinese with English abstract).
- Fan, W.M., Wang, Y.J., Zhang, Y.H., Zhang, Y.Z., Jourdan, F., Zi, J.W., Liu, H.C., 2015. Paleotethyan subduction process revealed from Triassic blueschists in the Lancang tectonic belt of Southwest China. *Tectonophysics* 662, 95–108.
- Ferré, E.C., Bernard, E.L., 2001. Geodynamic significance of early orogenic high-K crustal and mantle melts: example of the Corsica Batholith. *Lithos* 59, 47–67.
- Frost, B.R., Arculus, R.J., Barnes, C.G., Collins, W.J., Ellis, D.J., Frost, C.D., 2001. A geochemical classification of granitic rocks. *J. Petrol.* 42, 2033–2048.
- Frost, C.D., Frost, B.R., 2011. On ferroan (A-type) granitoids: their compositional variability and modes of origin. *J. Petrol.* 52, 39–53.
- Grimes, C.B., John, B.E., Kelemen, P.B., Mazdab, F.K., Wooden, J.L., Cheadle, M.J., Hanghoj, K., Schwartz, J.J., 2007. Trace element chemistry of zircons from oceanic crust: a method for distinguishing detrital zircon provenance. *Geology* 35, 643–646.
- Halliday, A.N., Davidson, J.P., Hildreth, W., Holden, P., 1991. Modelling the petrogenesis of high Rb/Sr silicic magmas. *Chem. Geol.* 92, 107–114.
- Hanson, G.N., 1978. The application of trace elements to the petrogenesis of igneous rocks of granitic composition. *Earth Planet. Sci. Lett.* 38, 26–43.
- Harris, N.B.W., Pearce, J.A., Tindle, A.G., 1986. Geochemical characteristics of collision-zone magmatism. In: Coward, M.P., Ries, A.C. (Eds.), *Collision Tectonics. Special Publication*, Geological Society of London, pp. 67–81.
- Hennig, D., Lehmann, B., Frei, D., Belyatsky, B., Zhao, X.F., Cabral, A.R., Zeng, P.S., Zhou, M.F., Schmidt, K., 2009. Early Permian seafloor to continental arc magmatism in the eastern Paleo-Tethys: U-Pb age and Nd-Sr isotope data from the southern Lancangjiang zone, Yunnan, China. *Lithos* 113, 408–422.
- Holtz, F., Johannes, W., 1991. Genesis of peraluminous granites: I. Experimental investigation of melt composition at 3 and 5 kb and various H_2O activities. *J. Petrol.* 32, 909–934.
- Hoskin, P.W.O., Schaltegger, U., 2003. The composition of zircon and igneous and metamorphic petrogenesis. *Rev. Mineral. Geochem.* 53, 27–62.
- Hu, P.Y., Li, C., Li, J., Wang, M., Xie, C.M., Wu, Y.W., 2014. Zircon U-Pb-Hf isotopes and whole-rock geochemistry of gneissic granites from the Jitang complex in Leiwuqi area, eastern Tibet, China: Record of the closure of the Paleo-Tethys Ocean. *Tectonophysics* 623, 83–99.
- Hu, Z.C., Gao, S., Liu, Y.S., Hu, S.H., Chen, H.H., Yuan, H.L., 2008a. Signal enhancement in laser ablation ICP-MS by addition of nitrogen in the central channel gas. *J. Anal. At. Spectrom.* 23, 1093–1101.
- Hu, Z.C., Liu, Y.S., Gao, S., Hu, S.H., Dietiker, R., Günther, D., 2008b. A local aerosol extraction strategy for the determination of the aerosol composition in laser ablation inductively coupled plasma mass spectrometry. *J. Anal. At. Spectrom.* 23, 1192–1203.
- Hu, Z.C., Liu, Y.S., Gao, S., Liu, W.G., Zhang, W., Tong, X.R., Lin, L., Zong, K.Q., Li, M., Chen, H.H., Zhou, L., Yang, L., 2012. Improved in situ Hf isotope ratio analysis of zircon using newly designed X skimmer cone and jet sample cone in combination with the addition of nitrogen by laser ablation multiple collector ICP-MS. *J. Anal. At. Spectrom.* 27, 1391–1399.
- Huang, H.Q., Li, X.H., Li, W.X., Li, Z.X., 2011. Formation of high $\delta^{18}\text{O}$ fayalite-bearing A-type granite by high-temperature melting of granulitic metasedimentary rocks, southern China. *Geology* 39, 903–906.
- Janoušek, V., Finger, F., Roberts, M., Frýda, J., Pin, C., Dolejs, D., 2004. Deciphering the petrogenesis of deeply buried granites: whole-rock geochemical constraints on the origin of largely undepleted felsic granulites from the Moldanubian Zone of the Bohemian Massif. *Trans. Royal Soc. Edinburgh-Earth Sci.* 389, 141–159.
- Jian, P., Liu, D.Y., Kröner, A., Zhang, Q., Wang, Y.Z., Sun, X.M., Zhang, W., 2009a. Devonian to Permian plate tectonic cycle of the Paleo-Tethys Orogen in southwest China (I): Geochemistry of ophiolites, arc/back-arc assemblages and within-plate igneous rocks. *Lithos* 113, 748–766.

- Jian, P., Liu, D.Y., Kröner, A., Zhang, Q., Wang, Y.Z., Sun, X.M., Zhang, W., 2009b. Devonian to Permian plate tectonic cycle of the Paleo-Tethys Orogen in southwest China (II): Insights from zircon ages of ophiolites, arc/back-arc assemblages and within-plate igneous rocks and generation of the Emeishan CFB province. *Lithos* 113, 767–784.
- Jiang, X.Y., Luo, J.C., Guo, J., Wu, K., Zhang, Z.K., Sun, W.D., Xia, X.P., 2018. Geochemistry of I- and A-type granites of the Qingyang-Jiuhanshan complex, eastern China: Insights into early cretaceous multistage magmatism. *Lithos* 316–317, 278–294.
- Kamber, B.S., Collerson, K.D., 2000. Role of 'hidden' deeply subducted slabs in mantle depletion. *Chem. Geol.* 166, 241–254.
- Karsli, O., Chen, B., Aydin, F., Şen, C., 2007. Geochemical and Sr-Nd-Pb isotopic compositions of the Eocene Dölek and Sarıçek Plutons, Eastern Turkey: implications for magma interaction in the genesis of high-K calc-alkaline granitoids in a post-collision extensional setting. *Lithos* 98, 67–96.
- Karsli, O., Dokuz, A., Aydin, F., Uysal, İ., Şengün, F., Kandemir, R., Santos, J.F., Andersen, T., 2020. Tracking the timing of Neotethyan oceanic slab break-off: Geochronology and geochemistry of the quartz diorite porphyries, NE Turkey. *J. Asian Earth Sci.* 200, 104456.
- Kemp, A.I.S., Wormald, R.J., Whitehouse, M.J., Price, R.C., 2005. Hf isotopes in zircon reveal contrasting sources and crystallization histories for alkaline to peralkaline granites of Temora, southeastern Australia. *Geology* 33, 797–800.
- King, P.L., White, A.J.R., Chappell, B.W., Allen, C.M., 1997. Characterization and origin of aluminous A-type granites from the Lachlan Fold Belt, southeastern Australia. *J. Petrol.* 38, 371–391.
- Kong, H.L., Dong, G.C., Mo, X.X., Zhao, Z.D., Zhu, D.C., Wang, S., Li, R., Wang, Q.L., 2012. Petrogenesis of Lincang granites in Sanjiang area of western Yunnan Province: Constraints from geochemistry, zircon U-Pb geochronology and Hf isotope. *Acta Petrologica Sinica* 28, 1438–1452 (in Chinese with English abstract).
- Kröner, A., Santosh, M., Wong, J., 2012. Zircon ages and Hf isotopic systematics reveal vestiges of Mesoproterozoic to Archaean crust within the late Neoproterozoic–Cambrian high-grade terrain of southernmost India. *Gondwana Res.* 21, 876–886.
- Lee, C.-T.A., Bachmann, O., 2014. How important is the role of crystal fractionation in making intermediate magmas? Insights from Zr and P systematics. *Earth Planet. Sci. Lett.* 393, 266–274.
- Li, C., 2008. A review on 20 years' study of the Longmu Co-Shuanghu-Lancang river suture zone in Qinghai-Xizang (Tibet) Plateau. *Geol. Rev.* 54, 105–119 (in Chinese with English abstract).
- Li, G.M., Li, J.X., Zhao, J.X., Qin, K.Z., Cao, M.J., Evans, N.J., 2015. Petrogenesis and tectonic setting of Triassic granitoids in the Qiangtang terrane, central Tibet: evidence from U-Pb ages, petrochemistry and Sr-Nd-Hf isotopes. *J. Asian Earth Sci.* 105, 443–455.
- Li, X.H., Li, Z.X., Li, W.X., Liu, Y., Yuan, C., Wei, G., Qi, C., 2007. U-Pb zircon, geochemical and Sr-Nd-Hf isotopic constraints on age and origin of Jurassic I- and A-type granites from Central Guangdong, SE China: a major igneous event in response to foaming of a subducted flat-slab? *Lithos* 96, 186–204.
- Liegeois, J.P., Navez, J., Hertogen, J., Black, R., 1998. Contrasting origin of post-collisional high-K calc-alkaline and shoshonitic versus alkaline and peralkaline granitoids: the use of sliding normalization. *Lithos* 45, 1–28.
- Liu, D., Zhao, Z., Zhu, D.C., Niu, Y., Harrison, T.M., 2014. Zircon xenocrysts in Tibetan ultrapotassic magmas: imaging the deep crust through time. *Geology* 42, 43–46.
- Liu, D.Z., Wang, G.Z., Li, Y.G., Zhu, L.D., Tao, X.F., Cu, X.H., 1999. New progress in isotopic geochronology of the Northern Section of Lancangjiang zone. *Regional Geol. China* 18, 334–335 (in Chinese).
- Liu, H., Wang, B.D., Ma, L., Gao, R., Chen, L., Li, X.B., Wang, L.Q., 2016. Late Triassic syn-exhumation magmatism in central Qiangtang, Tibet: evidence from the Sangehu adakitic rocks. *J. Asian Earth Sci.* 132, 9–24.
- Ludwig, K.R., 2003. ISOPLOT 3.0: A geochronological toolkit for Microsoft Excel. Special Publication No. 4. Berkeley Geochronology Center.
- Luo, W., Li, Y.G., Fei, G.C., Peng, J., 2016. Geochemical characteristics of the Biluoqueshan granitoid pluton in western Yunnan and their geological implications. *Geol. Exploration* 52, 261–270 (in Chinese with English abstract).
- Ma, X.X., Shu, L.S., Meert, J.G., 2015. Early Permian slab breakoff in the Chinese Tianshan belt inferred from the post-collisional granitoids. *Gondwana Res.* 27, 228–243.
- Mao, Q.G., Xiao, W.J., Fang, T.H., Windley, B.F., Sun, M., Ao, S.J., Zhang, J.E., Huang, X. K., 2014. Geochronology, geochemistry and petrogenesis of Early Permian alkaline magmatism in the Eastern Tianshan: implications for tectonics of the Southern Altaiids. *Lithos* 190–191, 37–51.
- Metcalfe, I., 2002. Permian tectonic framework and palaeogeography of SE Asia. *J. Asian Earth Sci.* 20, 551–566.
- Metcalfe, I., 2013. Gondwana dispersion and Asian accretion: Tectonic and palaeogeographic evolution of eastern Tethys. *J. Asian Earth Sci.* 66, 1–33.
- Middlemost, E.A.K., 1994. Naming materials in the magma/igneous rock system. *Earth Sci. Rev.* 37, 215–224.
- Miller, C.F., 1985. Are strongly peraluminous magmas derived from pelitic sedimentary sources? *J. Geol.* 93, 673–689.
- Miller, C.F., McDowell, S.M., Mapes, R.W., 2003. Hot and cold granites? Implications of zircon saturation temperatures and preservation of inheritance. *Geology* 31, 529–532.
- Mo, X.X., Deng, J.F., Lu, F.X., 1994. Volcanism and the evolution of Tethys in Sanjiang area, southwestern China. *J. SE Asian Earth Sci.* 9, 325–333.
- Mo, X.X., Lu, F.X., Shen, S.Y., 1993. Sanjiang Tethyan volcanism and related mineralization. Geological Publishing House, Beijing (in Chinese).
- Nie, F., Dong, G.C., Mo, X.X., Zhu, D.C., Dong, M.L., Wang, X., 2012. Geochemistry, zircon U-Pb chronology of the Triassic granites in the Changning-Menglian suture zone and their implications. *Acta Petrologica Sinica* 28, 1465–1476 (in Chinese with English abstract).
- Pan, G.T., Xu, Q., Hou, Z.Q., Wang, L.Q., Du, D.X., Mo, X.X., Li, D.M., Wang, M.J., Li, X. Z., Jiang, X.S., Hu, Y.Z., 2003. Archipelagic orogenesis, metallogenetic systems and assessment of the mineral resources along the Nujiang–Lancangjiang–Jinshajiang area in southwestern China. Geological Publishing House, Beijing, 420p. (in Chinese with English abstract).
- Patino Douce, A.E., 1996. Effects of pressure and H₂O content on the compositions of primary crustal melts. *Transactions of the Royal Society of Edinburgh. Earth Sci.* 87, 11–21.
- Patino Douce, A.E., 1997. Generation of metaluminous A-type granitoids by low-pressure melting of calc-alkaline granitoids. *Geology* 25, 743–746.
- Patino Douce, A.E., 1999. What do experiments tell us about the relative contributions of crust and mantle to the origins of granitic magmas? In: Castro, A., Fernandez, C., Vigneresse, J.L. (Eds.), *Understanding Granites: Integrating New and Classical Techniques*. Geological Society of London, Special Publication 168, 55–75.
- Pearce, J.A., 1996. Sources and settings of granitic rocks. *Episodes* 19, 120–125.
- Pearce, J.A., Harris, N.B.W., Tindle, A.G., 1984. Trace element discrimination diagrams for the tectonic interpretation of granitic rocks. *J. Petrol.* 25, 956–983.
- Peng, T.P., Wang, Y.J., Fan, W.M., Liu, D.Y., Shi, Y.R., Miao, L.C., 2006. SHRIMP zircon U-Pb geochronology of early Mesozoic felsic igneous rocks from the southern Lancangjiang and its tectonic implications. *Sci. China (Series D)* 49, 1032–1042.
- Peng, T.P., Wilde, S.A., Wang, Y.J., Fan, W.M., Peng, B.X., 2013. Mid-Triassic felsic igneous rocks from the southern Lancangjiang Zone, SW China: petrogenesis and implications for the evolution of Paleo-Tethys. *Lithos* 168–169, 15–32.
- Peng, T.P., Zhao, G.C., Fan, W.M., Peng, B.X., Mao, Y.S., 2015. Late Triassic granitic magmatism in the Eastern Qiangtang, Eastern Tibetan Plateau: Geochronology, petrogenesis and implications for the tectonic evolution of the Paleo-Tethys. *Gondwana Res.* 27, 1497–1508.
- Petford, N., Atherton, M., 1996. Na-rich partial melts from newly underplated basaltic crust: The Cordillera Blanca Batholith, Peru. *J. Petrol.* 37, 1491–1521.
- Pfänder, J.A., Münker, C., Stracke, A., Mezger, K., 2007. Nb/Ta and Zr/Hf in ocean island basalts—Implications for crust–mantle differentiation and the fate of Niobium. *Earth Planet. Sci. Lett.* 254, 158–172.
- Pitcher, W.S., 1983. Granite types and tectonic environment. In: Hsu, K. (Ed.), *Mountain Building Processes*. Academic Press, London, pp. 19–40.
- Rickwood, P.C., 1989. Boundary lines within petrologic diagrams which use oxides of major and minor elements. *Lithos* 22, 247–263.
- Roberts, M.P., Clemens, J.D., 1993. Origin of high-potassium, calc-alkaline, I-type granitoids. *Geology* 21, 825–828.
- Rollinson, H.R., 1993. *Using Geochemical Data: Evaluation, Presentation, Interpretation (Longman Geochemistry)*. Longman Publishing Group, London, p. 343p.
- Rudnick, R.L., Gao, S., 2003. Composition of the Continental Crust. 3. Elsevier-Pergamon, Oxford, 64p.
- Sami, M., Ntaflos, T., Farahat, E.S., Mohamed, H.A., Hauzenberger, C., Ahmed, A.F., 2018. Petrogenesis and geodynamic implications of Ediacaran highly fractionated A-type granitoids in the north Arabian-Nubian shield (Egypt): Constraints from whole rock geochemistry and Sr-Nd isotopes. *Lithos* 304–307, 329–346.
- Sengör, A.M.C., 1987. Tectonics of the Tethysides: Orogenic collage development in a collisional setting. *Annu. Rev. Earth Planet. Sci.* 15, 213–244.
- Sengör, A.M.C., 1990. Plate tectonics and orogenic research after 25 years: A Tethyan perspective. *Earth Sci. Rev.* 27 (1–2), 1–201.
- Sisson, T.W., Ratajczak, K., Hankins, W.B., Glazner, A.F., 2005. Voluminous granitic magmas from common basaltic sources. *Contrib. Miner. Petrol.* 148, 635–661.
- Stampfli, G.M., Borel, G.D., 2002. A plate tectonic model for the Paleozoic and Mesozoic constrained by dynamic plate boundaries and restored synthetic oceanic isochrons. *Earth Planet. Sci. Lett.* 196, 17–33.
- Su, J., Huang, J.G., Jiang, Y.L., 2014. Geochemical Characteristics and Tectonic Significance of Manghuai Formation Volcanic Rock in Biluo Snow Mountain Area in Western Yunnan. *Hennan Sci.* 32, 588–594 (in Chinese with English abstract).
- Sun, S.S., McDonough, W.F., 1989. Chemical and isotopic systematics of oceanic basalts: implications for mantle composition and processes. *Geol. Soc., London, Special Publ.* 42, 313–345.
- Sylvester, P.J., 1998. Post-collisional strongly peraluminous granites. *Lithos* 45, 29–44.
- Sylvester, P.J., 1989. Post-collisional alkaline granites. *J. Geol.* 97, 261–280.
- Tao, Y., Bi, X.W., Li, C.S., Hu, R.Z., Li, Y.B., Liao, M.Y., 2014. Geochronology, petrogenesis and tectonic significance of the Jitang granitic pluton in eastern Tibet, SW China. *Lithos* 184–187, 314–323.
- Tian, D.X., Yang, H., Ge, W.C., Zhang, Y.L., Chen, J.S., Chen, H.J., Yun, X.Y., 2018. Petrogenesis and tectonic implications of Late Carboniferous continental arc high-K granites in the Dongwuqi area, central Inner Mongolia, North China. *J. Asian Earth Sci.* 167, 82–102.
- Topuz, G., Candan, O., Zack, T., Chen, F.K., Li, Q.L., 2019. Origin and significance of Early Miocene high-potassium I-type granite plutonism in the East Anatolian plateau (the Taşlıçay intrusion). *Lithos* 348–349, 10520.
- Wang, B.D., Wang, L.Q., Qiangba, Z., Zeng, Q.G., Zhang, W.P., Wang, D.B., Cheng, W.H., 2011. Early Triassic collision of northern Lancangjiang suture: geochronological, geochemical and Hf isotope evidences from the granitic gneiss in Leiwuqi area, East Tibet. *Acta Petrologica Sinica* 27, 2752–2762 (in Chinese with English Abstract).
- Wang, C.M., Bagas, L., Chen, J.Y., Yang, L.F., Zhang, D., Du, B., Shi, K.X., 2018a. The genesis of the Liancheng Cu-Mo deposit in the Lanping Basin of SW China: Constraints from geology, fluid inclusions, and Cu-S-H-O isotopes. *Ore Geol. Rev.* 92, 113–128.
- Wang, C.M., Bagas, L., Lu, Y.J., Santosh, M., Du, B., McCuaig, T.C., 2016. Terrane boundary and spatio-temporal distribution of ore deposits in the Sanjiang Tethyan Orogen: Insights from zircon Hf-isotopic mapping. *Earth Sci. Rev.* 156, 39–65.

- Wang, C.M., Deng, J., Carranza, E.J.M., Lai, X.R., 2014a. Nature, diversity and temporal-spatial distributions of sediment-hosted Pb-Zn deposits in China. *Ore Geol. Rev.* 56, 327–351.
- Wang, C.M., Deng, J., Carranza, E.J.M., Santosh, M., 2014b. Tin metallogenesis associated with granitoids in the southwest Sanjiang Tethyan Domain: Nature, types, and tectonic setting. *Gondwana Res.* 26, 576–593.
- Wang, C.M., Deng, J., Lu, Y.J., Bagas, L., Kemp, A.I.S., McCuaig, T.C., 2015a. Age, nature, and origin of Ordovician Zhibenshan granite from the Baoshan terrane in the Sanjiang region and its significance for understanding Proto-Tethys evolution. *Internal Geol. Rev.* 57, 1922–1939.
- Wang, C.M., Deng, J., Santosh, M., McCuaig, T.C., Lu, Y.J., Carranza, E.J.M., Wang, Q.F., 2015b. Age and origin of the Bulangshan and Mengsong granitoids and their significance for post-collisional tectonics in the Changning-Menglian Paleo-Tethys Orogen. *J. Asian Earth Sci.* 113, 656–676.
- Wang, C.M., Yang, L.F., Bagas, L., Evans, N., Chen, J.Y., Du, B., 2018b. Mineralization processes at the giant Jinding Zn-Pb deposit, Lanping Basin, Sanjiang Tethys Orogen: Evidence from in-situ trace element analysis of pyrite and marcasite. *Geol. J.* 53, 1279–1294.
- Wang, F., Liu, F.L., Liu, P.H., Shi, J.R., Cai, J., 2014c. Petrogenesis of Lincang granites in the south of Lancangjiang area: Constrain from geochemistry and zircon U-Pb geochronology. *Acta Petrologica Sinica* 30, 3034–3050 (in Chinese with English abstract).
- Wang, X., Metcalfe, I., Jian, P., He, L., Wang, C., 2000. The Jinshajiang-Ailaoshan Suture Zone, China: tectonostratigraphy, age and evolution. *J. Asian Earth Sci.* 18, 675–690.
- Wang, X.Y., Wang, S.F., Wang, C., Tang, W.K., 2018c. Permo-Triassic arc-like granitoids along the northern Lancangjiang zone, eastern Tibet: Age, geochemistry, Sr-Nd-Hf isotopes, and tectonic implications. *Lithos* 308–309, 278–293.
- Wang, Y.J., Xing, X.W., Cawood, P.A., Lai, S.C., Xia, X.P., Fan, W.M., Liu, H.C., Zhang, F., 2013. Petrogenesis of early Paleozoic peraluminous granite in the Sibumasu Block of SW Yunnan and diachronous accretionary orogenesis along the northern margin of Gondwana. *Lithos* 182, 67–85.
- Wang, Y.J., Zhang, A.M., Fan, W.M., Peng, T.P., Zhang, F.F., Zhang, Y.H., Bi, X.W., 2010. Petrogenesis of late Triassic post-collisional basaltic rocks of the Lancangjiang tectonic zone, southwest China, and tectonic implications for the evolution of the eastern Paleo-Tethys: geochronological and geochemical constraints. *Lithos* 120, 529–546.
- Watson, E.B., Harrison, T.M., 1983. Zircon saturation revisited: temperature and composition effects in a variety of crustal magma types. *Earth Planet. Sci. Lett.* 64, 295–304.
- Wei, C., Qi, X.X., Chang, Y.L., Ji, F.B., Zhang, S.Q., 2016. Identification on age of xiaodingxi formation volcanic rocks in central-southern lancangjiang orogeny and its tectonic implication. *Acta Geol. Sin.* 90, 3192–3214 (in Chinese with English abstract).
- Whalen, J.B., Currie, K.L., Chappell, B.W., 1987. A-type granites: geochemical characteristics, discrimination and petrogenesis. *Contrib. Miner. Petrol.* 95, 407–419.
- Wilson, B.M., 2007. Igneous Petrogenesis: A Global Tectonic Approach. Springer, Berlin, p. 416p.
- Wu, F.Y., Li, X.H., Yang, J.H., Zheng, Y.F., 2007. Discussions on the petrogenesis of granites. *Acta Petrologica Sinica* 23, 1217–1238 (in Chinese with English abstract).
- Wu, F.Y., Liu, X.C., Ji, W.Q., Wang, J.M., Yang, L., 2017. Highly fractionated granites: Recognition and research. *Sci. China-Earth Sci.* 60, 1201–1219.
- Wu, F.Y., Sun, D.Y., Li, H.M., Jahn, B.M., Wilde, S., 2002. A-type granites in northeastern China: age and geochemical constraints on their petrogenesis. *Chem. Geol.* 187, 143–173.
- Wu, H.R., Boulter, C.A., Ke, B.J., Stow, D.A.V., Wang, Z.C., 1995. The Changning-Menglian suture zone: a segment of the major Cathaysian-Gondwana divide in Southeast Asia. *Tectonophysics* 242, 267–280.
- Xin, D., Yang, T.N., Liang, M.J., Xue, C.D., Han, X., Liao, C., Tang, J., 2018. Syn-subduction crustal shortening produced a magmatic flare-up in middle Sanjiang Orogenic Belt, southeastern Tibet Plateau: Evidence from geochronology, geochemistry, and structural geology. *Gondwana Res.* 62, 93–111.
- Xu, M.H., Xue, C.D., Yang, T.N., Wu, J., Liao, C., Tang, J., Liang, M.J., Xin, D., 2016. LA-ICP-MS zircon U-Pb geochronology of the ore-bearing volcanic rocks in the Dazong copper orefield on the western margin of Lanping basin, western Yunnan, and its geological implications. *Acta Petrologica et Mineralogica* 35, 735–750 (in Chinese with English Abstract).
- Xu, W., Liu, F.L., Dong, Y.S., 2020. Cambrian to Triassic geodynamic evolution of central Qiangtang, Tibet. *Earth-Sci. Rev.* 201, 103083.
- Yang, L.F., Wang, C.M., Bagas, L., Du, B., Zhang, D., 2019. Mesozoic-Cenozoic sedimentary rock records and applications for provenance of sediments and affiliation of the Simao terrane, SW China. *Int. Geol. Rev.* 61, 2291–2312.
- Yang, L.F., Wang, C.M., Du, B., Chen, Q., He, Z.C., Zhu, J.X., 2020. Sequence and petrogenesis of the volcanic rocks from the middle Sanjiang Tethys Orogen, SW China: Implications for the Sanjiang Paleo-Tethyan evolution. *Geol. J.* 55, 6235–6254.
- Yang, T.N., Liang, M.J., Fan, J.W., Shi, P.L., Zhang, H.R., Hou, Z.Q., 2014. Paleogene sedimentation, volcanism and deformation in eastern Tibet: Evidence from structures, geochemistry and zircon U-Pb dating in the Jian-Chuan basin, SW China. *Gondwana Res.* 26, 521–535.
- YNBGMR (Yunnan Bureau Geological Mineral Resource), 1990. Regional Geology of Yunnan Province. Geological Publishing House, Beijing, 729p. (in Chinese with English abstract).
- Yuan, C., Sun, M., Xiao, W.J., Li, X.H., Chen, H.L., Lin, S.F., Xia, X.P., Long, X.P., 2007. Accretionary orogenesis of the Chinese Altai: Insights from Paleozoic granitoids. *Chem. Geol.* 242, 22–39.
- Zeng, W.T., Sun, Z.B., Zhou, K., Wu, J.L., Huang, L., Zhao, J.T., 2018. U-Pb dating of the detrital zircons in the dark dioritic enclaves from the Lincang granites in Mengku, Shuangjiang, western Yunnan and its geological significance. *Sedimentary Geol. Tethyan Geol.* 38, 23–36 (in Chinese with English abstract).
- Zhai, Q.G., Chung, S.L., Tang, Y., Hu, P.Y., Jin, X.C., Wang, J., Wang, H.T., Wang, K.L., Lee, H.Y., 2019. Late Carboniferous ophiolites from the southern Lancangjiang belt, SW China: Implication for the arc-back-arc system in the eastern Paleo-Tethys. *Lithos* 344–345, 134–146.
- Zhang, B., Zhang, J.J., Chang, Z.F., Wang, X.X., Cai, F.L., Lai, Q.Z., 2012. The Biluoqieshan transpressive deformation zone monitored by synkinematic plutons, around the Eastern Himalayan Syntaxis. *Tectonophysics* 574–575, 158–180.
- Zhang, H., Yu, Y.S., Wang, X.M., He, H., Xiao, P., Wang, F.M., 2017. Zircon U-Pb geochronology and geological significance of volcanic rocks from the western margin of Lanping Basin, Sanjiang Orogenic Belt, China. *Acta Mineralogica Sinica* 27, 596–607 (in Chinese with English Abstract).
- Zhao, F., Li, G.J., Zhang, P.F., Wang, C.B., Sun, Z.B., Tang, X., 2018a. Petrogenesis and tectonic implications of the Lincang batholith in the Sanjiang, Southwest China: Constraints by geochemistry, zircon U-Pb chronology and Hf isotope. *Acta Mineralogica Sinica* 34, 1397–1412 (in Chinese with English abstract).
- Zhao, Z., Wu, H., Lu, L., Yu, J.Q., Wu, Y.J., 2018b. The Late Triassic I-Type Granites from the Longmu Co-Shuanghu Suture Zone in the interior of Tibetan Plateau, China: petrogenesis and implication for slab break-off. *Acta Geologica Sinica (English Edition)* 92, 935–951.
- Zhong, D.L., 1998. Paleo-Tethyan Orogenic Belt in western Sichuan and western Yunnan. Science Press, Beijing, 231p. (in Chinese with English abstract).
- Zhu, R.Z., Lai, S.C., Qin, J.F., Zhao, S.W., Wang, J.B., 2017. Late Early-Cretaceous quartz diorite–granodiorite–monzogranite association from the Gaoligong belt, southeastern Tibet Plateau: Chemical variations and geodynamic implications. *Lithos* 288–289, 311–325.